Investigation of a Mobile Damping Robot for Electric Transmission Lines

Andrew C. Choi

Thesis submitted to the Faculty of the
Virginia Polytechnic Institute and State University
in partial fulfillment of the requirements for the degree of

Master of Science
in
Mechanical Engineering

Oumar R. Barry, Chair
Shima Shahab
Lei Zuo

May 5, 2023
Blacksburg, Virginia

Keywords: vibration, vibration control, mobile robots

Investigation of a Mobile Damping Robot for Electric Transmission Lines

Andrew C. Choi

(ABSTRACT)

Electric transmission lines suffer from many hazards, including wind-induced vibrations (WIV), which can lead to fatigue failure of the transmission conductors. Current vibration mitigation methods do not adequately address WIV because they overwhelmingly rely on narrow-band fixed absorbers. A mobile damping robot (MDR) can overcome the limitations of these fixed absorbers by actively transporting them to locations of highest amplitude on the cable; i.e., antinodes. These antinodes are where the absorbers can most efficiently remove energy from the system. While analyses have been performed for vibration absorbers on transmission line conductors, they have not been in the context of a mobile damping robot (MDR). There is a need to investigate the potential impact of the MDR on a transmission line and the resulting implications for the MDR's development. In this thesis, we explore the dynamics of a power line conductor through finite element analysis (FEA) and modal testing. We perform numerical analysis in MATLAB® using equations of motion obtained via Hamilton's Principle. We discuss the design and validation of an appropriate test bench and MDR prototype. We also experimentally investigate the ability of the MDR prototype to transport a mass along a conductor to antinode locations. Experimental results indicate that the damping robot is indeed able to navigate to cable locations of highest amplitude corresponding to antinodes. We then conclude and discuss future work. The insights gained from this research lay a foundation to guide further development of the MDR. Through this

work, we are better able to define the operating conditions of the MDR, which will facilitate the creation of a more robust, adaptable control framework for expanded capability.

Investigation of a Mobile Damping Robot for Electric Transmission Lines

Andrew C. Choi

(GENERAL AUDIENCE ABSTRACT)

Power transmission lines are important civil structures used to deliver electricity across the nation. However, these lines are subject to an array of hazards that can damage them. One such hazard is vibration due to wind, which can cause fatigue damage, leading to power line failure and outages. A popular form of vibration control is the use of a fixed vibration absorber, which has significant limitations. A mobile damping robot (MDR) can greatly improve upon the efficiency of these absorbers by transporting them to optimal locations along the power line. This thesis explores the utility and feasibility of an MDR to do so. We investigate with the help of engineering software and establish the conditions for experimentation. Our research suggests that the MDR prototype we constructed can autonomously navigate itself along the power line to optimal locations. This research will guide improvements to the MDR so that it can be more effective under real-world conditions.

Dedication

To my wife and the light of my life, Tanya

Acknowledgments

I thank my wife for her endless love and support. I thank my advisor, Dr. Barry, for his guidance, for inviting me to join his lab, and for the opportunity to work on such a meaningful project. I am grateful for my committee members Dr. Lei Zuo and Dr. Shima Shahab. I am also grateful to Dr. Jiamin Wang and PhD candidate Paul-Camille Kakou for their mentorship during my graduate studies. And I thank all my labmates for their advice and aid as well.

Contents

List of Figures

List of Tables

List of Abbreviations

FPVA Fixed Passive Vibration Absorber - A mass suspended to a power line cable to dissipate energy and mitigate vibration.

MDR Mobile Damping Robot - Robot cable to transporting passive absorbers along an electric transmission conductor cable.

WIV Wind-Induced Vibrations - Vibration caused by von Karman vortex shedding

Chapter 1

Introduction

1.1 Motivation

The electric grid is a crucial component of national infrastructure. Electricity must be transmitted across long distances to reach end users from the location where it is generated. This requires a network of interconnected transmission lines that span the country, as seen in Figure 1.1. Given their great importance, the protection and maintenance of these transmission lines are key priorities. The need for proper asset management is especially germane as the U.S. electric grid ages in the face of increasing demand due to climate change. The energy sector was given a C- rating from the American Society of Civil Engineers in 2021 [3]. Parts of the electric grid are over 100 years old, and 70% of transmission lines are over 30 years old [3]. Meanwhile, the grid is under additional stress with the rise of electric vehicles and other technologies [3, 4]. In fact, a Princeton study found that the U.S. may need to triple its transmission infrastructure by 2050 to meet projected demand from the move toward renewable technologies [4].

Unfortunately, current solutions do not adequately protect overhead transmission lines against structural damage caused by vibrations due to vortex shedding. As fluid flows across a cylindrical body, such wind blowing across a transmission line conductor, it leaves an unsteady non-symmetric wake of staggered vortices [50]. These von Karman Streets are shown in Figure 1.2. The force of the alternating vortices can cause the conductor to oscillate. If

Figure 1.1: Overhead electric transmission lines. Image courtesy of Kreuzschnabel/Wikimedia Commons [44].

the vortices alternate at the right frequency, the conductor will vibrate at resonance. These wind-induced vibrations (WIV) are typically Aeolian vibrations caused by wind speeds of 1-7 m/s and in the range of 3-150 Hz [10, 17, 21, 34, 37, 38, 56, 59].

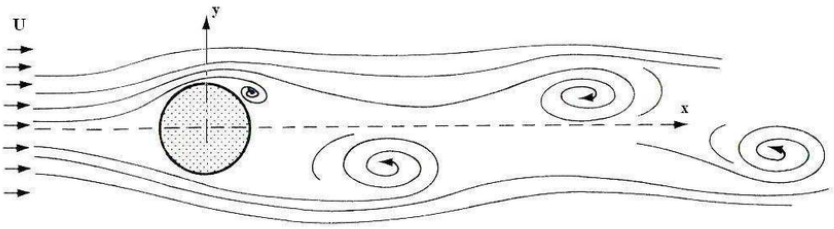

Figure 1.2: Vortex shedding. Image courtesy of Cunha [29].

WIV can lead to fatigue failure of the transmission conductor due to high cycles of bending stress [16, 22, 35, 36, 45, 56, 57]. These failures serve to undermine public safety and often result in considerable economic loss. Even a simple outage can cost data centers nearly

$9000 per minute [3]. While in worst case scenarios, transmission line faliure can lead to catastrophes such as the 2018 Camp Fire in California [25], as shown in Figure 1.3. This wildfire led to the deaths of 84 people and cost tens of billions of dollars in damages [52].

Figure 1.3: 2018 California Camp Fire. Image courtesy of NASA. [ref]

With so much at stake, utilities are under tremendous pressure to safeguard these transmission assets. However, the difficulty and expense of preventing fatigue damage and performing inspection to determine the condition of overhead transmission lines is a source of increasing strain. This is evidenced by the uptick in transmission infrastructure spending from $9.1 billion in 2000 to $40 billion in 2019 [60]. These growing pressures have led to an effort to modernize the electric grid and improve resilience.

1.2 Present Methodology

1.2.1 Vibration Absorbers

The state-of-the-art solution to mitigating WIV is to attach Fixed Passive Vibration Absorbers (FPVAs) (Figure 1.5) to the transmission line conductors. FPVAs dissipate the

energy from WIV, thereby reducing the amplitude of the vibrations in an effort to keep the cable below its endurance limit [18, 19, 56, 62, 63]. While relatively affordable and readily available, FPVAs are fundamentally inefficient at certain resonance frequencies due to their inability to change location. The ideal locations for FPVAs are at the antinodes of the conductor, where they are maximally effective at dissipating energy. However, these locations vary with wind conditions, and FPVAs can not adapt to these changes by relocating themselves to the new antinode locations.

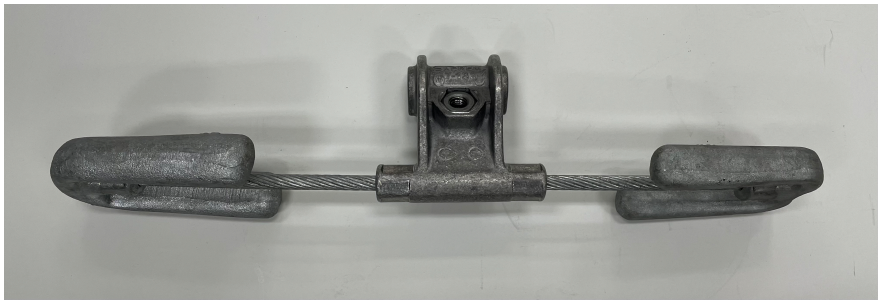

Figure 1.4: A common form of an FPVA - Stockbridge Damper.

Although studies have been performed to optimize FPVA placement, it is not possible to place FPVAs near antinode locations for all resonance frequencies in the range of Aeolian vibrations [11, 12, 48, 58]. For example, Barry et al found that optimal placement for a fixed damper highly depends on low or high wind speeds [11]. Additionally, FPVA locations may also coincide with nodes where they are the least efficient at dissipating energy, causing the absorbers to lose their effectiveness. In fact, if an FPVA is fixed at a node, it may be worse than having no absorber at all due to the increased strain caused by its mass [48, 58]. Although the odds of a fixed absorber's placement coinciding with the location of a node are low, the potential damage is quite high. Even low frequency vibrations for just minutes each day would result in several megacycles each year, with most conductors seeing far more cycles [35]. An FPVA's effectiveness is further dependent on its ability to match the resonance frequencies of the conductor to which it is attached, typically being limited to

just a couple matching frequencies [18, 21, 31, 48, 63]. Even the most advanced FPVAs can only match six natural frequencies of the conductor [63].

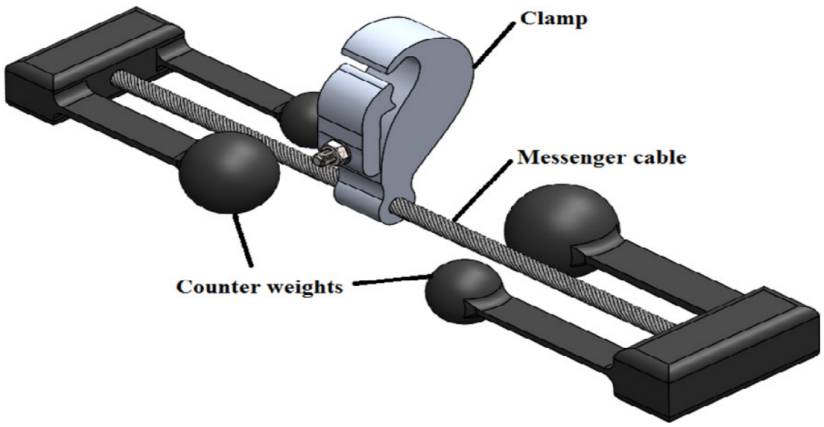

Figure 1.5: A novel damper cable of matching six resonance frequencies of a conductor.

1.2.2 Inspection Robots

Inspection robots are a rapidly growing field making inroads in various industries, and the inspection robot market grew 31.6% from its size in 2020 to $1.237B in 2021 [1]. These robots can reduce the cost and difficulty of inspection that utilities are required to perform due on transmission lines due to WIV and other hazards. PG&E's Electric Transmission Preventive Maintenance Manual notes that some patrols must be done every quarter with more detailed inspections due annually [54]. These inspections have traditionally been performed via foot patrol or by helicopter [43, 61]. Both techniques are typically expensive and laborious, and they can be dangerous as well. For these reasons, numerous inspection robots have been developed for transmission lines [2, 26, 31, 47, 49, 51, 55, 67]. However, the implementation of these robots has been hindered by their high cost, high power demands, and considerable weight and size. For instance, the LineSpyX robot (Figure 1.6) weighs 25kg [33]. While Unmanned Aerial Vehicles (UAVs) have grown in use, they also face significant limitations

such as short flight time, minimum clearance requirements, the need for operator control, and restricted flight beyond visual line of sight [61, 66]. Furthermore, none of these options are designed for autonomy and vibration control.

Figure 1.6: LineSpyX power line robot [33]

1.2.3 Undergrounding

To mitigate the risk of adverse events due to transmission line failure, utilities are turning more frequently to buying these lines underground [46]. However, this can cost up to four times more than construction of overhead transmission lines at nearly $4M per mile for undergrounding [30]. Approval for this option can also be difficult due to the rate increases incurred by the end consumer [30]. Moreover, it is impractical to perform undergrounding beyond a small minority of transmission lines, as the U.S. has over 600,000 miles of transmission lines [3].

1.3 Mobile Damping Robot

It is clear that current solutions for transmission line management have severe limitations. To overcome these shortcomings, Barry et al [16] have proposed a novel mobile damping robot (MDR) for vibration control, as shown in Figure 1.7. The MDR would actively transport vibration absorbers to intelligently and adaptively suppress WIV. The MDR was also specifically conceived for long-term mounting and autonomous navigation, filling a critical technology gap in existing offerings for utilities that struggle to maintain the integrity of transmission lines. While some researchers have previously explored the concept of moving dampers in other domains [32, 65], Barry et al were the first to investigate moving dampers in the context of power line WIV suppression [16]. The MDR would be capable of compensating for changing wind characteristics to automatically re-position to the locations of antinodes. This would optimally reduce vibration amplitude, thereby preventing fatigue damage and extending conductor lifespans.

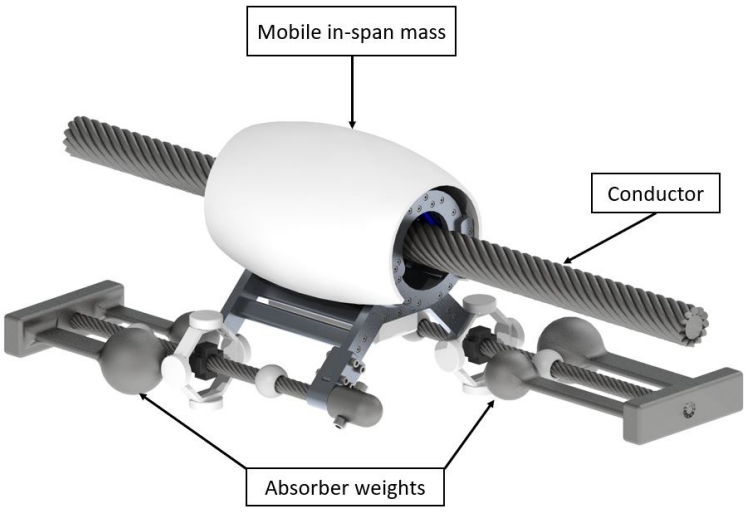

Figure 1.7: Conceptual design model of the mobile damping robot.

The MDR was further explored by Kakou et al, who found that mobile absorbers improved

vibration control at least tenfold when compared to traditional FPVAs [53], as seen in Figure 1.8. They also utilized feedback control to adapt the MDR's motion profile to the input excitation to further demonstrate the efficacy of mobile absorbers [40, 41, 42]. However, the work by Kakou et al required knowledge of the cable parameters and excitation frequency for the MDR to locate and travel to the theoretical antinode positions. Since the presence of the MDR on the conductor impacts cable dynamics, operation of the MDR based on theoretical knowledge would likely result in the robot traveling to an incorrect position in real-world conditions.

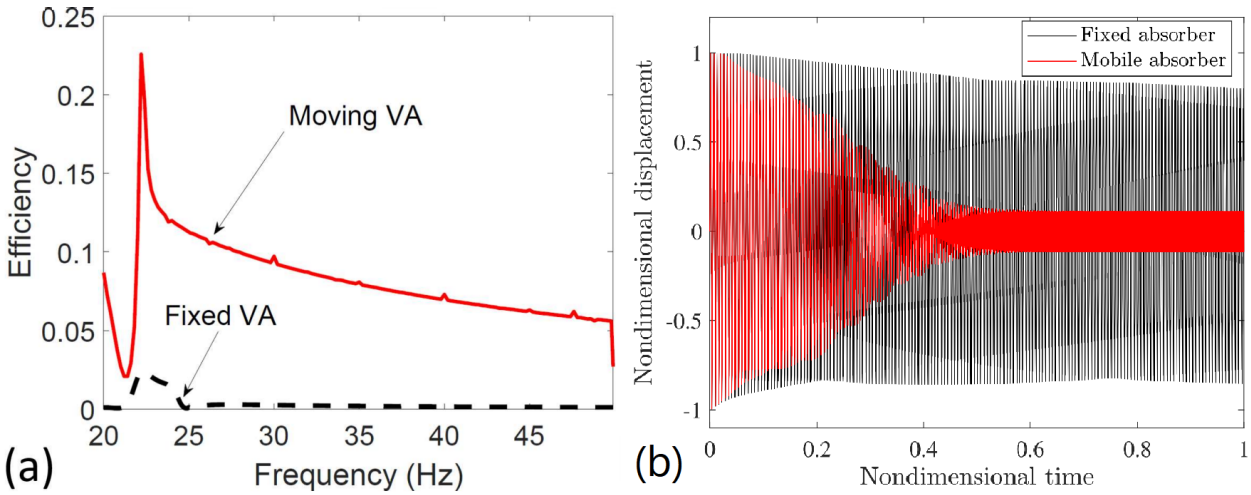

Figure 1.8: Simulation results showing performance of a fixed vs moving vibration absorber: (a) Efficiency, (b) Displacement.

Therefore, a critical research need exists to examine how the presence of the MDR itself affects conductor vibrations and behavior, as well as the MDR's ability to adapt to shifting wind conditions. In this work, we demonstrate the ability of a mobile damping robot to navigate to the resultant antinodes of a power line conductor with no a priori knowledge. This lays the groundwork to build out a complete control scheme for adaptive real-time operation. In the future, inspection capabilities could also be added to avoid the aforementioned difficulty of the inspections in Section 1.2.2. The development of the MDR will ultimately

empower utilities beyond performing inspection and meeting related regulatory requirements by equipping them to better protect and inspect their transmission assets. This would lead to improved resilience and reliability of the electric grid to shape a more secure energy future.

1.4 List of Contributions

The contributions of this thesis are summarized below:

1. A review of the challenges facing the electric grid and the current solutions in use. This review is used to highlight the need for the development of a mobile damping robot.

2. The design and construction of a modular test bench for experimentation. The test bench allows for the results from testing and validation of prototypes to be generalized to the larger conductors used in industry. It also allows for a variety of experimental conditions.

3. The design and fabrication of a mobile damping robot prototype. The prototype affords us the opportunity to test our hypotheses and ensure that the robot does improve vibrations relative to fixed absorbers.

4. Experimental validation of an antinode tracking algorithm to autonomously navigate the robot prototype to the antinodes of the cable. The algorithm allows the robot to deliver its promised value and outperform fixed absorbers.

1.5 Thesis Structure

The remainder of the thesis is structured as follows:

Chapter 2 presents both the mathematical model used to represent our experimental setup and the numerical analyses using Ansys and Matlab. This chapter also discusses the progression of the test bench used for the experiments.

Chapter 3 outlines the development of the MDR prototype's mechanical design, component selection, and programming.

Chapter 4 reviews the experiments performed to test the prototype's performance and discusses the results.

Chapter 5 summarizes the work undertaken thus far and outlines future work to be done.

1.6 Selected Publications

Disclaimer: Content from the following publications are used throughout this work.

Conference Proceedings

1. **Choi, A.**, Kakou, P. C., & Barry, O. (2022, August). Considerations for the Testing and Validation of a Mobile Damping Robot for Overhead Power Lines. In International Design Engineering Technical Conferences and Computers and Information in Engineering Conference (Vol. 86311, p. V010T10A026). American Society of Mechanical Engineers.

2. **Choi, A.** & Barry, O. (2023, August). Testing and Validation of a Mobile Damping Robot for Power Lines. In International Design Engineering Technical Conferences

and Computers and Information in Engineering Conference. American Society of Mechanical Engineers.

Journal Publications

3. **Choi, A.**, Gulbahce, E., Kakou, P., & Barry, O. (2023). Testing and Validation of Mobile Damping Robot Antinode Tracking Algorithm for Overhead Transmission Lines. Engineering Structures.*

*Preparing to Submit

Chapter 2

Exploration of a Suitable Experimental Test Bench

This chapter details the process of improving the test bench used for experimentation and testing with the MDR prototype. We first outlined the mathematical model of the system. Then we corrected clear deficits in the original existing test bench and performed experiments in an attempt better understand the cable dynamics. However, we did not find good agreement between the numerical and experimental results, which indicated that the test bench was not appropriate for further use. Therefore, we designed and constructed an improved test bench, which was then validated using similar experiments.

2.1 Mathematical Model

A mathematical model of the system was used for analysis in MATLAB®. The motion of a power line conductor can be obtained via Newton's Second Law, but it is difficult to define the mathematical equation of a conductor's motion because of its complex structure. Thus, it can be simplified as a solid cylindrical body with a homogeneous structure throughout its cross-sectional area [6, 64]. The conductor was modeled as vibration of a simply supported Euler-Bernoulli beam with axial tension, and the MDR was modeled as an attached spring-mass-damper system [7, 8, 9, 10, 12, 13, 14, 17, 23, 24]. A representation of the mathematical

model is depicted in Figure 2.1. Here, x is the horizontal placement of the MDR on the conductor span, m_i is the in-span robot mass, k is the spring constant of the absorber, c is the damping coefficient of the absorber, m_d is the suspended absorber mass, and y_d is the vertical displacement of the suspended absorber mass. Unlike in the work of Kakou et al [39, 40, 42], the MDR was not modeled as a moving vibration absorber. This is due to our focus on the impact of the MDR while stationary at various locations along the cable rather than while traveling. Similarly, energy harvesting was also excluded from the scope of this work.

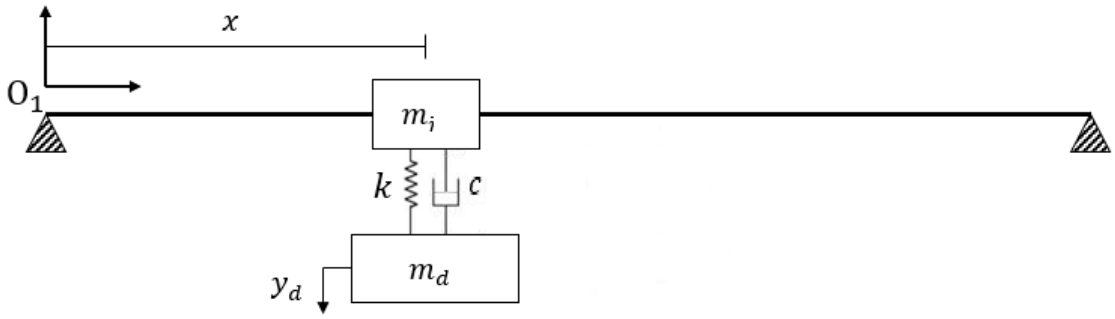

Figure 2.1: Schematic of the MDR on a conductor cable.

The position vectors of the beam, in-span mass, and suspended mass were first defined to represent their positions and displacements. The time derivatives of the position vectors were then derived and used to further derive the velocity vectors. The velocity vectors were used to find the kinetic energy of the system elements, the sum of which define the kinetic energy of the system as a whole. The potential energy was defined for the system elements with consideration of restoring forces. The application of Hamilton's Principle to these equations results in the following equation of motion

$$EIy'''' + m\ddot{y} + Ty'' = F(x,t) - (F_1 + F_2)D(x,t) \tag{2.1}$$

Here $F(x,t)$ is an excitation force at a single point expressed in the form of

$$F(t) = f_0 sin(\omega_e t) \tag{2.2}$$

where f_0 is the amplitude of the force, and ω_e is the input frequency. F1, F2 and D(x,t) are expressed as

$$F_1 = m_i \ddot{y} \tag{2.3}$$

$$F_2 = k(y - y_d) + c(\dot{y} - \dot{y_d}) \tag{2.4}$$

$$D(x,t) = \delta(x - x_r) \tag{2.5}$$

Finally, the transverse displacement of the suspended mass is given to be

$$m_d \ddot{y}_d - F_2 = 0 \tag{2.6}$$

Although used for simulation and validating the experimental test bench, the mathematical model was not a large focus of our work, as it has already been well-established. Also, contrary to the work of Kakou et al [42], our aim was to use the model to validate an experimental test setup. Therefore, only the vertical displacement of the fixed damper case needed to be considered, and the equations of motion for the MDR's movement were disregarded.

2.2 Original Test Bench

The original test bench was constructed by the senior design team and used for minor experiments regarding locomotion and clamping of the senior design prototype. However, there were many shortcomings of the test bench that the team had left unaddressed, so many

improvements had to be made before testing could begin. Firstly, the tensioning winch was moved to be mid-line of the tower since its previous asymmetric mounting caused torsion to the tower, which led to deformation of a vertical strut. This strut was realigned and reinforced. Secondly, the cable needed to be replaced since there were numerous kinks and bends on the previous cable that affected its behavior under excitation. Thirdly, the mounts were replaced to better secure the cable to the towers, since the previous method required the use of wooden blocks as shims due to the ill-fitting oversized hose clamps that were used. Lastly, the clamp for the electrodynamic shaker was redesigned to be much smaller since its previous width created a large contact area that negatively impacted the vibration of the cable. Some of these deficits are depicted in Figure 2.2 below.

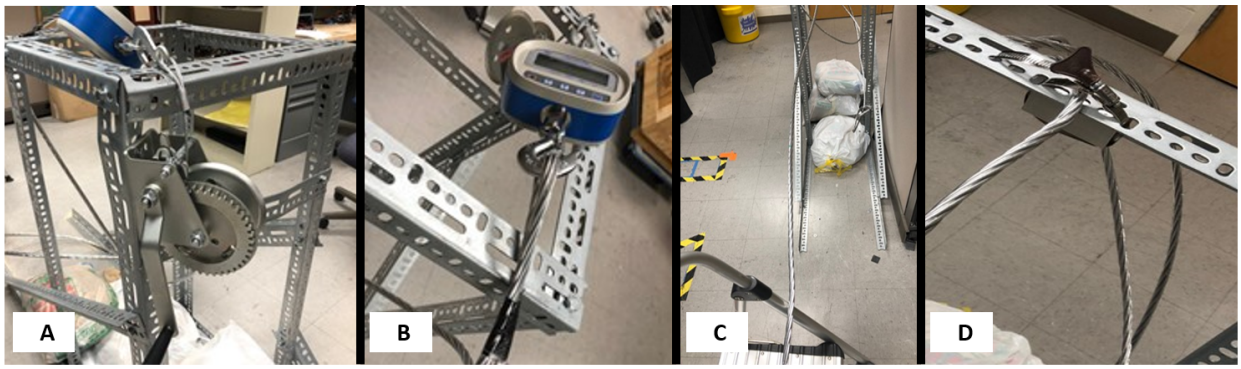

Figure 2.2: Deficits in original test bench. A) Deformed strut, B) Misaligned cable, C Kinked cable, D) Improperly sized connector

2.2.1 Preliminary Investigation

Initial experiments were performed to gain an understanding of the cable dynamics and determine the effects of suspended masses within the vibration loops. This served as a precursor to future experiments and provided foundational knowledge needed to guide development of the MDR antinode tracking algorithm. We also wanted to verify experimentally that our understanding of the cable's behavior with a supended mass was correct; namely, that an

untuned mass at the location of a node would worsen vibrations, while an untuned mass at the location of an antinode would improve vibrations.

The experiments were performed using an exciter (LDS Test and Measurement V408 electrodynamic shaker), an analyzer (Siemens SCADAS Mobile), and a signal conditioner (Bruel & Kjaer LDS LPA100 amplifier), as depicted in Figure 2.3. Additionally, an accelerometer (PCB Piezotronics 352C33) was used to measure the input acceleration of the shaker as a reference with another accelerometer (PCB Piezotronics YT352C34) placed at an antinode of the mode shape corresponding to the forcing frequency. Siemens Simcenter Testlab software was used to interface with the hardware and record data.

Figure 2.3: Experiment hardware. (1) exciter, (2) analyzer, (3) signal conditioner.

Figure 2.4 depicts a schematic of the experimental setup. The two towers were composed of slotted aluminum angles. The cable was an Aster All Aluminum Conductor (AAC). The cable was secured to the towers using p-clamps and two-hole straps. A Haul-Master hand winch on one tower was used to tension the cable. The tension was measured using a PCE-CS 300 force gauge on the same tower. The electrodynamic shaker was attached to the cable at midspan with a clamp [9]. The tensioning and excitation portions of the setup are depicted in Figure 2.5.

A stepped sine output was used to obtain the frequency response of the cable across a

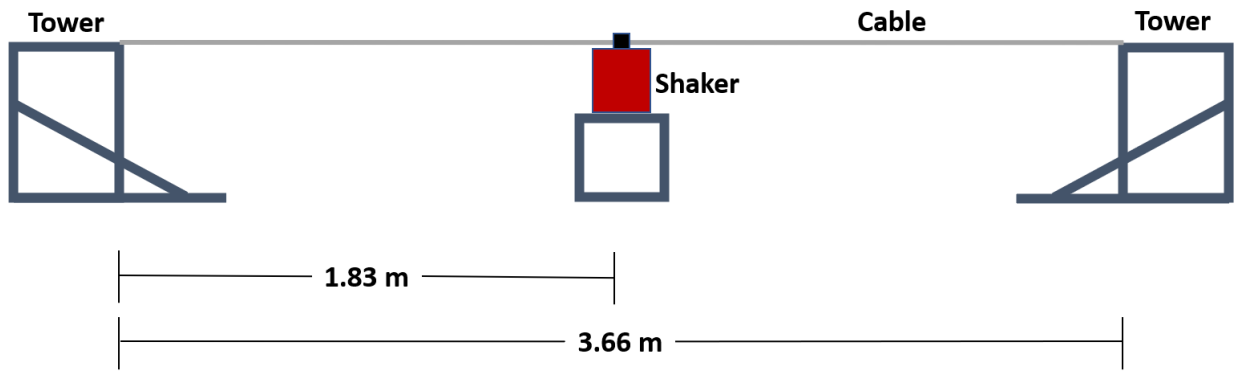

Figure 2.4: Diagram of the experimental setup.

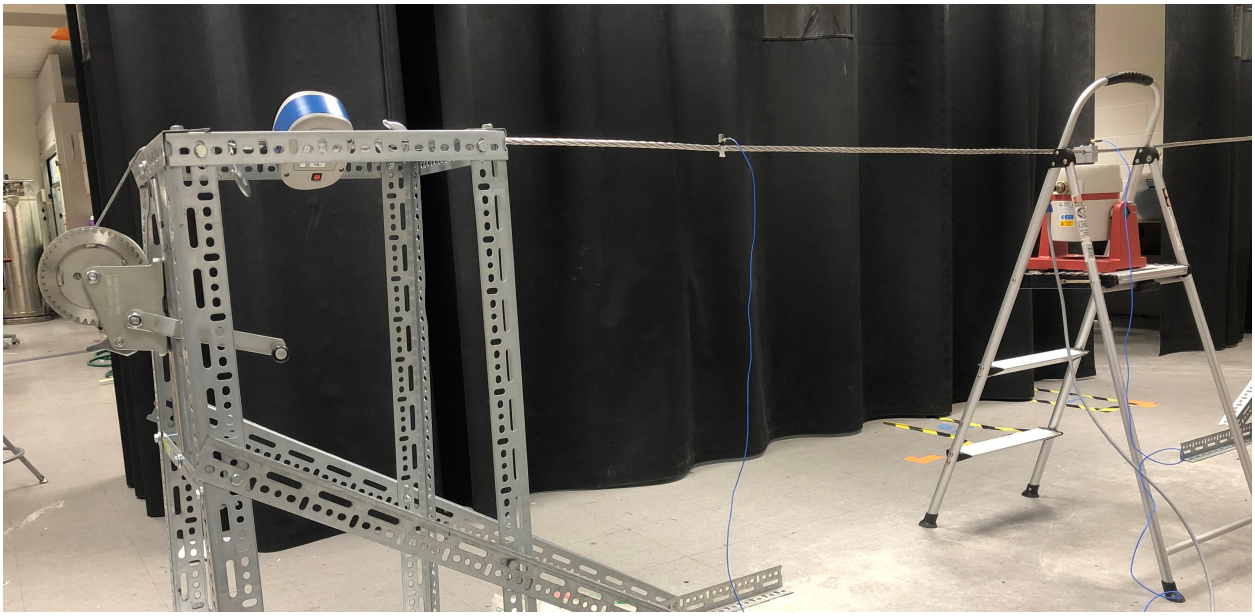

Figure 2.5: Experimental setup. The right non-tensioning tower is to the right of frame.

range of 10-25 Hz with a step increment of 0.01 Hz. Resonance in the frequency response function was best seen at the second mode shape around 12.6 Hz, which was verified by visual observation of the cable. This response suggested a fundamental frequency of 6.3 Hz. The fundamental frequency was verified to align with the theoretical value given by

$$f_n = \frac{1}{2L}\sqrt{\frac{T}{\rho A}} \tag{2.7}$$

where L is length of the cable span, T is the tension of the cable, and ρA is the mass per unit length. The full cable parameters are given in Table 2.1.

Table 2.1: Cable Parameters.

Parameter	**Value**	**Unit**
Mass	0.681	kg
Mass/Unit Length	0.186	kg/m
Length	3.66	m
Tension	395	N
Diameter	10.5	mm
Elasticity	71	GPa

When the constraints of the experimental setup were considered, it was desirable to perform testing at the third mode since it would provide access to an unbounded node (not attached to the tower or shaker). Testing at the fourth and fifth modes were also considered, but they were rejected due to the preference for a larger vibration loop length. The fundamental frequency indicated a theoretical third mode at 18.9 Hz, which was indicated by the FRF as well. When evaluated at this forcing frequency, the cable vibrated at high amplitude and clearly demonstrated a third mode shape. The loop lengths were found to be equal at 1.22 m per loop for each of three loops across the 3.66 m span.

Initially, the cable alone was tested with a sine output. The response of the cable was displayed as a time series in Testlab with real acceleration on the y-axis in m/s^2 and automatically adjusted to account for offset due to gravity. After data collection, the maximum accelerations were determined and plotted in Figure 2.7. As expected, the acceleration at the nodes was near zero, and the acceleration was highest at the antinode. Next, the mass corresponding to 5% of the cable mass was hung between the first node (tower-cable connection) and antinode of the first vibration loop of the cable. Acceleration data was collected at 0.305 m increments from the first node to the second node, for a total of five measurement

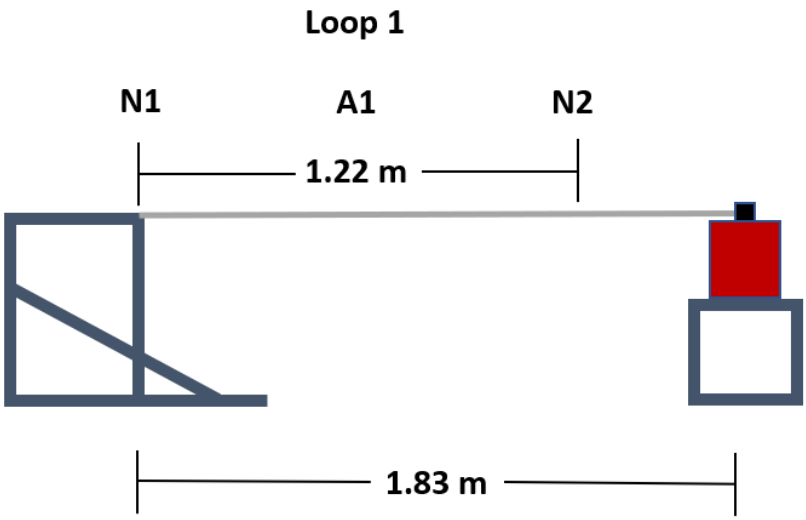

Figure 2.6: Diagram of the section used for testing. Nodes are denoted with an 'N' and antinodes are denoted with an 'A'. Loops are bounded by nodes.

locations. Then the mass was moved in 0.305 m increments to the second node for a total of four suspension locations. This resulted in a total of 20 data points per mass. This process was repeated for the 10%, 15%, 20%, and 25% masses for a total of 100 data points. The masses used are defined in Table 2.2.

Table 2.2: Values of suspended masses.

Target %	**5%**	**10%**	**15%**	**20%**	**25%**
Target Mass	34 g	68 g	102 g	136 g	170 g
Actual Mass	34.6 g	66.7 g	101.6 g	140.2 g	170.3 g
Actual %	5.1%	9.8%	14.9%	20.6%	25.0%
% Difference	1.7%	0.4%	0.4%	3.1%	0.2%

2.2.2 Analysis & Results

We simulated the acceleration of the system in MATLAB® using the ODE45 function. An approximation of n=5 was used, with the in-span and suspended masses independent of the

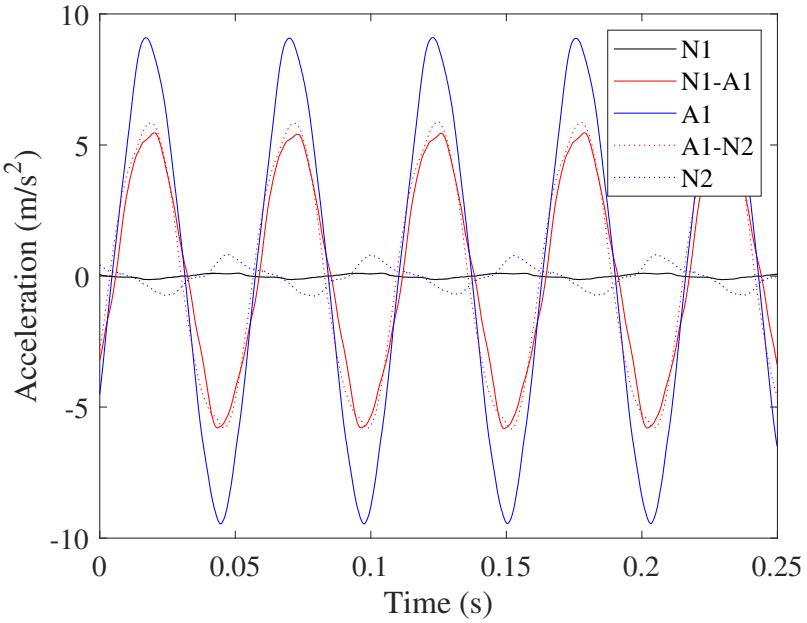

Figure 2.7: Acceleration values for the cable without any mass attached. Locations midway between nodes and the antinode are denoted with a dash. E.g., the position halfway between node 1 (N1) and antinode 1 (A1) is defined as N1-A1.

number of modes. The solution for the cable alone (Figure 2.8) showed that the 3rd mode dominated the response, as expected for the excitation frequency used. The modes were summed, and the numerical solution showed good agreement with the experimental result, as seen in Figure 2.9.

Solutions were then found for the cable with the suspended masses. The masses were simulated at the first antinode and second node locations. Although the initial simulation results above were promising, this additional modeling showed less agreement between the experimental and numerical findings. As seen in Figure 2.10, modeling produced decreasing acceleration in both cases. While the experiments demonstrated that placement of the masses at the antinode matched the numerical trend and reduced vibration, they also demonstrated the opposite trend for the mass placed at the node as acceleration actually increased slightly experimentally. Additionally, the scale of the acceleration changes for the mass placed at the

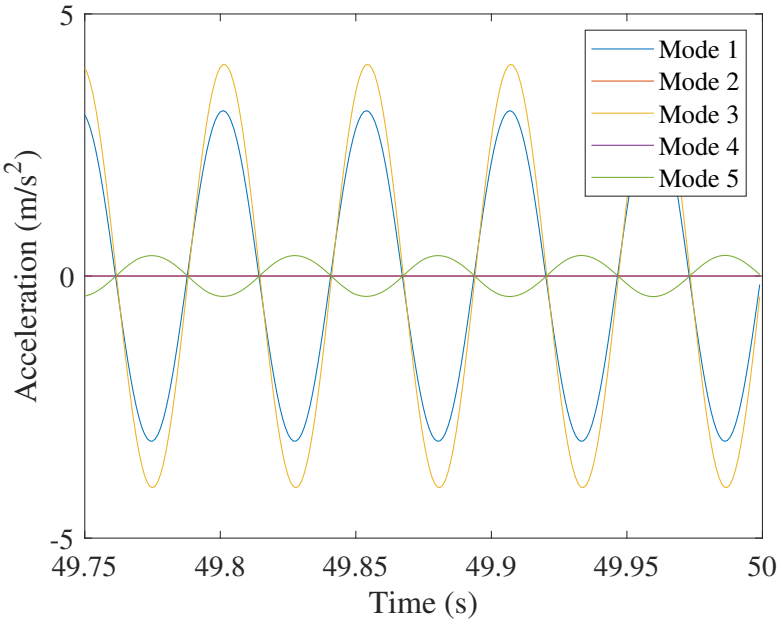

Figure 2.8: Acceleration for each composite mode of the cable's steady state response.

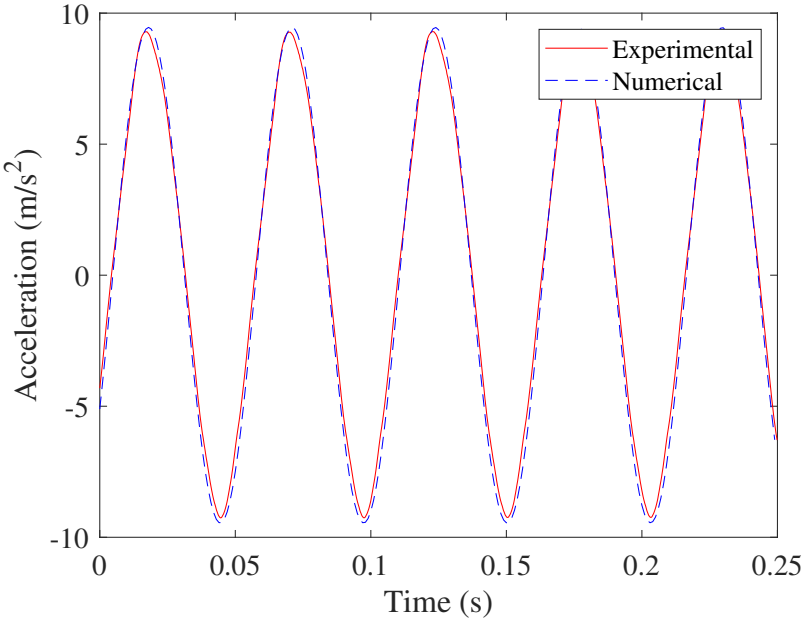

Figure 2.9: Comparison of the experimental acceleration and the summed numerical acceleration for the cable only as measured at the first antinode.

node was markedly different, with the numerical analysis producing much higher amplitudes and significantly larger changes for each increase in mass.

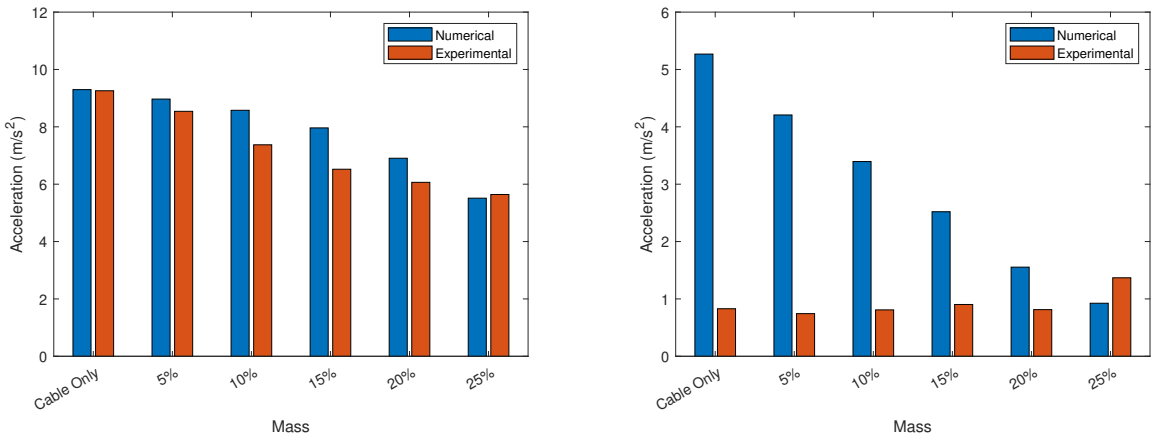

(a) Acceleration with mass and measurement at first antinode.

(b) Acceleration with mass and measurement at second node.

Figure 2.10: Comparison of numerical and experimental results for masses suspended at the location of a node and antinode.

This relationship between the numerical and experimental results was confirmed by the rest of the experiments. They consistently showed that there was a clear positive effect on cable vibration when a mass was placed at a antinode and a clear negative effect when a mass was placed at a node. We also observed that the addition of a mass to the vibration loop caused the node to shift inward toward the antinode. These shifts were mass dependent, as each increase in mass corresponded to an increasing leftward movement. The practical result of this effect was that larger masses created shorter loop lengths. Figure 2.11 depicts the shrinking effect of the vibration loops due to increasing mass. The white marking indicates the original node position at 1.22 m. The yellow marking indicates the new node position when the 5% mass was suspended at the antinode. Each subsequent rightward marking indicates the new node position for the remaining masses in ascending order. Note that the new locations of the node indicate by how much the loop has shortened. These results are summarized in Table 2.3.

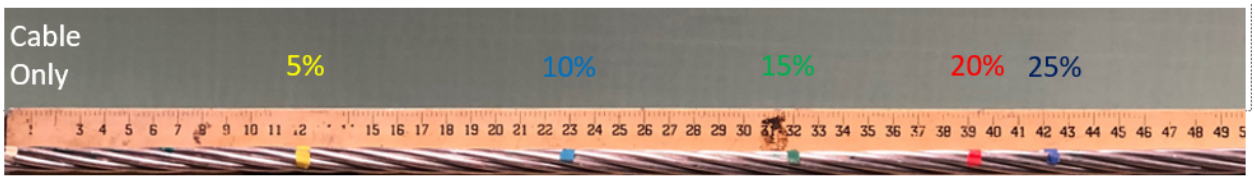

Figure 2.11: Distance by which the node shifted with addition of each mass to the cable.

Table 2.3: Node shifts. Deltas indicate the amount by which the loop length shortened due to the presence of the masses.

Mass %	**Color**	**Delta (cm)**	**Delta (%)**
5%	Yellow	∼12.25	∼10.0%
10%	Teal	∼23.0	∼18.9%
15%	Green	∼32.0	∼26.2%
20%	Red	∼39.25	∼32.2%
25%	Blue	∼42.25	∼34.6%

We verified these visual observations by taking acceleration readings at the new node locations. These measurements indicated that these were in fact new locations for the node. The accelerations aligned closely with one another as well as the acceleration at the original node for the cable only. These accelerations were also found to be significantly reduced from those same locations for the cable alone. As also briefly tested with the fifth mode shape to determine the effect of untuned masses on the vibration loops when there are two free nodes as opposed to one free node with a node connected to the tower. It was found that both nodes of the loop shifted inward, although in unequal fashion. The node nearer to the tower moved in relatively smaller increments while the node nearer to midspan moved in larger increments. While additional testing was attempted on a non-terminal loop at a higher order mode shape, the short cable span made it difficult to observe the effects on the cable, let alone properly measure them.

2.2.3 Discussion

The lack of congruence in the trends indicated that we could not validate the mathematical model for this experimental setup. This was despite making adjustments to the model the input force as harmonic excitation of a single frequency with a single point input midspan. We did not consider otherwise revising the mathematical model, as we knew that it had been well validated in the literature. From this preliminary work, it was clear that the experimental test bench needed to be completely redesigned due to poor agreement between the numerical and experimental results [27]. In such a case, any experimental results could not reasonably be extended to real world cables that have been previously shown to be modeled as a beam. These inconsistencies were largely attributed to 1) short cable span, 2) small cable diameter, and 3) low tension.

The short span necessitated that previous testing was performed at a low harmonic to ensure a large enough vibration loop length for testing. With excitation corresponding to the third mode shape, testing on the middle span was not feasible due to the placement of the shaker. This meant that there were non-ideal boundary conditions and that certain nodes were unavailable for measurement due to serving as attachment points. The impact of the masses on cable vibration was likely modified by proximity to the tower. The small diameter meant that the cable mass was also low, which would negatively impact the design of the MDR. As we saw in the previous section, even a relatively small mass of 101.6g resulted in the node shifting by over 25%. This would mean that any MDR prototype would have to be impractically lightweight. The low tension meant that cable would have too much slack, allowing small curvatures that could affect cable dynamics and the MDR's movement.

2.3 Final Test Bench

2.3.1 Improvements

The foremost consideration when designing the new test bench was modularity. Since we could not be sure that any specific set of cable parameters would match the Euler-Bernoulli beam model without an extensive parameterization study, we opted for a modular design to accommodate a number of different cables. T-slot aluminum framing was ideal for this aspect. To accommodate a longer cable length, additional ground rails could be inserted. To to accommodate a larger diameter, a number of clamps or other hardware could be used to connect to the tower rails. To increase the tension, various tensioning devices could be used. Also, additional supports could be added if static deflection became too high at higher tensions. A fixture attached within each tower would also allow the cable height to be individually adjusted. This would allow for testing at various angles as well as adjusting for the height of different shaker placements or robot sizes. A CAD drawing of the tower design is shown in Figure 2.12.

We used both the 80/20 Deflection Calculator and finite element analysis (FEA) and to ensure that there would be sufficient factor of safety for the forces we were expecting based on reasonable cable tensions. With the Deflection Calculator, we found just 0.49 mm of deflection at 3x our expected static load for the vertical members, even assuming maximum cable height, which would apply the most torque. In the same scenario, the deflection of the horizontal member was only 0.51 mm. We found similar low deflections in the range of fractions of a mm from our FEA simulations. As a precaution, the number of brackets used to secure joint connections were increased to be well beyond what was necessary to avoid any obvious points of failure.

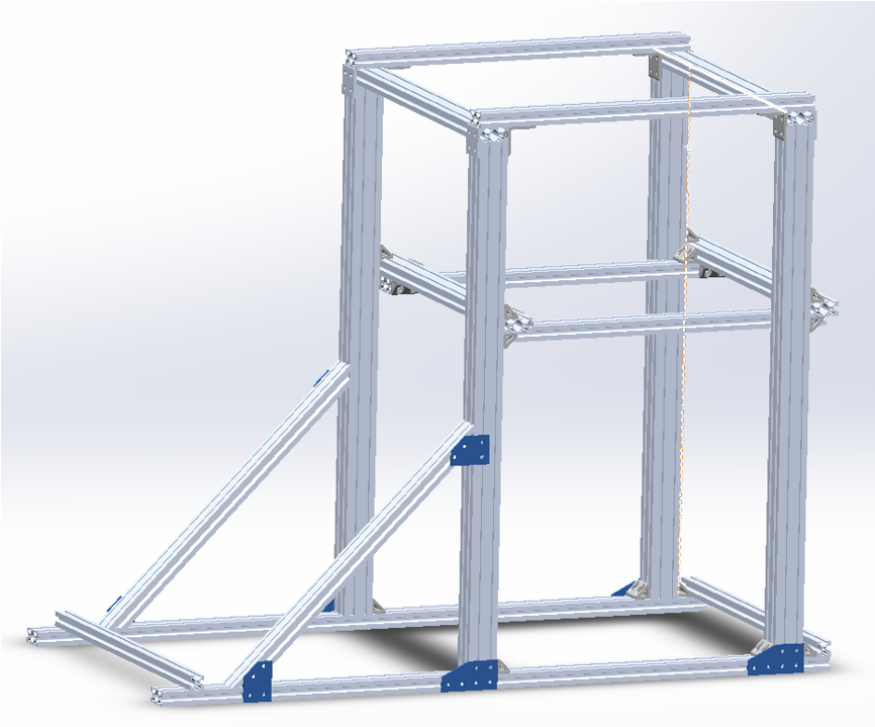

Figure 2.12: CAD model of the updated test bench tower.

A new cable with a larger diameter and longer length was also purchased. Table 2.4 gives the parameters of the new cable. The length was limited due to the constraints of the lab space.

Table 2.4: Cable Parameters.

Parameter	**Value**	**Unit**
Mass	2.56	kg
Mass/Unit Length	0.3493	kg/m
Length	7.32	m
Tension	872	N
Diameter	14.4	mm
Elasticity	71	GPa

The final physical setup is shown in Figure 2.13 and entailed securing the cable to two towers using p-clamps and two-hole straps. A Haul-Master hand winch was used to tension

the cable, as measured using a PCE-CS 300 force gauge. The towers were constructed using T-slot aluminum framing, and the cable was a Sneezewart All Aluminum Conductor (AAC). The shaker was rigidly attached to the cable at midspan with a clamp.

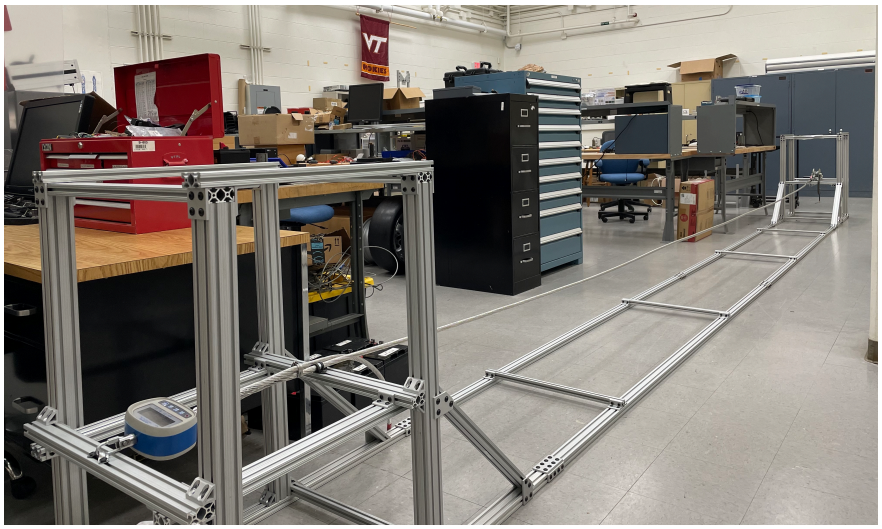

Figure 2.13: New test bench.

We also switched to the use of a laser vibrometer to complement the use of accelerometers mounted to the cable. This allowed for multiple points to be tested in quick succession, obviating the need for remounting accelerometers. It also gave us the ability to scan points that an accelerometer could not be mounted to (e.g., robot in the way).

2.3.2 Bare Conductor Dynamics

To ensure that the new test bench adequately matched our mathematical model, we first sought to compare the natural frequencies of the bare conductor between various methods. When beam theory is considered, the analytical natural frequencies can be obtained using Equation 2.3.2 [15, 28, 64].

$$w_n = \frac{n}{2L}\sqrt{\frac{T}{\rho A} + (\frac{n\pi}{L})^2\frac{EI}{\rho A}} \tag{2.8}$$

Here, n is an integer denoting the mode number ($n = 1, 2, ...$), L is the cable length, T is the cable tension,, ρA is the mass per unit length of the cable, and EI is the flexural rigidity of the cable. While the flexural rigidity varies along the span, it can be simplified to a uniform value for modeling. In the case that EI is quite small, the conductor can behave like a string [64]. When flexural properties are ignored (zero or very low), Equation 2.3.2 turns into

$$w_f = \frac{n}{2L}\sqrt{\frac{T}{\rho A}} \tag{2.9}$$

A complement to analytical solutions is the use of finite element analysis (FEA) to obtain the natural frequencies of a structure such as the test cable. FEA was carried out using commercial ANSYS software, and BEAM188 element [5] was used for modeling [15, 28, 64]. The boundary conditions were modeled as simply supported on both ends, and gravity was applied to the model for more realistic behavior. Firstly, static structural analysis was carried out using an APDL command that satisfied the experimental tension. Then, pre-stressed modal analysis was realized to obtain the natural frequencies of the bare conductor. The dimensional parameters and material properties used for both analytical and finite element modeling matched those of the test cable as given in Table 2.4 in Section 2.3.1. Lastly, the experimental modal frequencies were obtained using an impact hammer to compare with the analytical and numerical results. These were verified using white noise excitation and a swept sine output with a step increment of 0.1 Hz. The results are presented in Table 2.5.

The results indicated that while the conductor could be modeled as a string, the beam model was more accurate. This was an encouraging result, as it suggested that the test bench had been improved enough to match the mathematical model. As previously mentioned, matching the mathematical model was important to ensure that our experimental findings would be generalizable to real world conditions, as cables in common use in industry were best modeled as Euler-Bernoulli beams.

Table 2.5: Analytical, Numerical, and Experimental Natural Frequencies of the Bare Conductor

Modes	**Analytical (String)**	**Analytical (Beam)**	**ANSYS (Beam)**	**Experimental**
1st	3.4142	3.4665	3.4677	3.88
2nd	6.8284	7.2450	7.2469	7.38
3rd	10.243	11.606	11.607	11.50
4th	13.657	16.756	16.756	15.47
5th	17.0642	22.839	22.840	19.94

2.3.3 Validation

The final steps to validate our test bench involved the performance of similar experiments to the original test bench. Namely, the suspension of untuned masses to points of interest along the cable to identify trends in conductor dynamics. The experiments were performed using an exciter (LDS Test and Measurement V408 electrodynamic shaker), an analyzer (Polytec Data Management System), and a signal conditioner (Bruel & Kjaer LDS LPA100 amplifier). A scanning vibrometer (PSV-500-3D) was placed above the cable to scan multiple points across vibration loops of the mode shape corresponding to the forcing frequency. The experimental setup and instruments used are depicted in Figure 2.14. Additionally, an accelerometer (PCB Piezotronics 352C33) was used to measure the input acceleration of the shaker as a reference. Polytec PSV Software was used to interface with the hardware and record data.

Figure 2.15 shows a schematic of the experimental setup for testing at the 8th harmonic, which was desirable due to accessible non-bounded vibration loops with lengths of nearly a meter. The 8th mode was selected since it best fit the constraints of the experimental setup while avoiding the pitfalls of earlier experiments. We used one half of the cable for testing due to the placement of the shaker at midspan. This configuration produced the most equal vibration loops at roughly 0.92 m each between two adjacent nodes. Loops 2 and 3, between

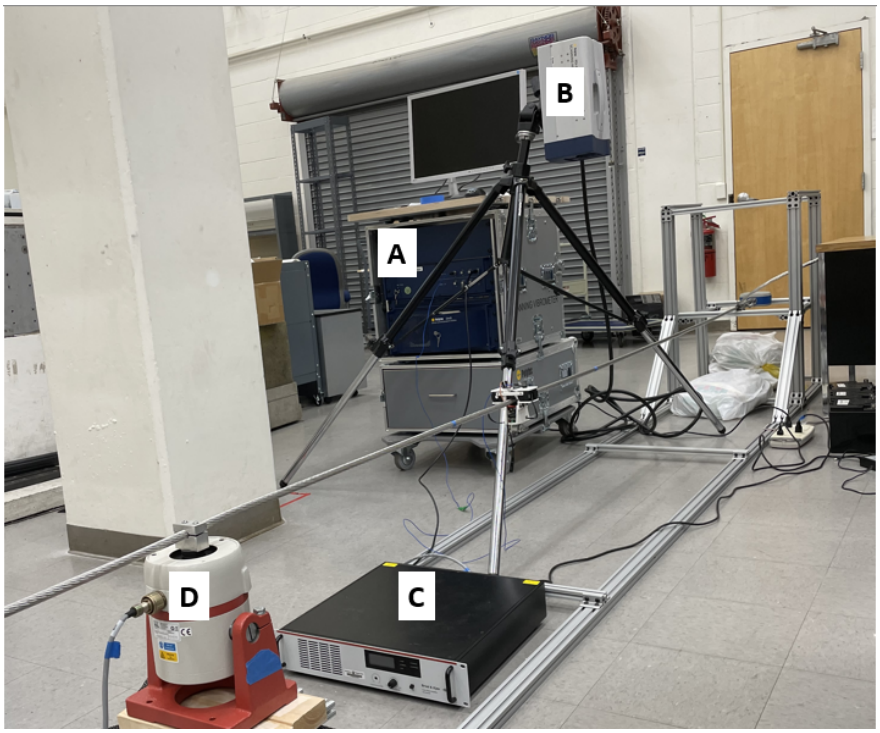

Figure 2.14: Experimental setup. Instruments useds: A) Analyzer, B) Scanning Head, C) Amplifier, D) Shaker.

N2 & N3 and N3 & N4 respectively, were used for testing. To avoid unwanted boundary conditions, we excluded the first and fourth loops from testing. A schematic of the section used is presented in Figure 2.16.

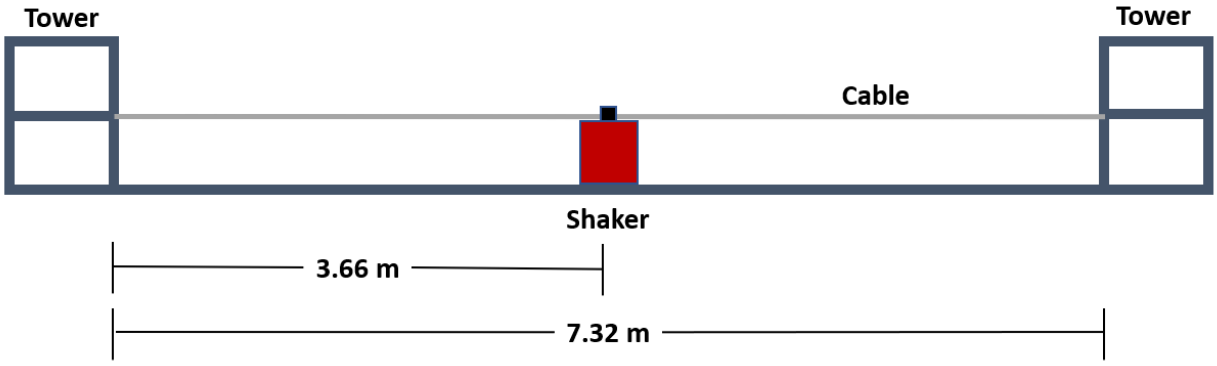

Figure 2.15: Experimental Setup

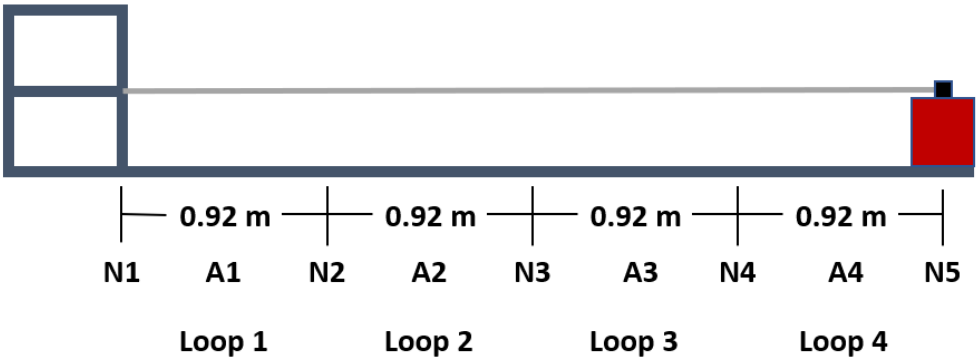

Figure 2.16: Schematic of the experimental setup. Nodes are denoted with an 'N' and antinodes are denoted with an 'A'. Loops are bounded by nodes.

We initially tested the bare conductor with a sine output of 32 Hz, corresponding to the previously selected 8th mode shape. This was easily verified by visual observation, as the cable vibrated at high amplitude and clearly demonstrated an eighth mode shape when evaluated at a forcing frequency of 32 Hz. The scanning head vibrometer was placed above the cable to measure the velocity at 11 points along a section of Loops 2 and 3. The response of the cable was displayed in PSV Acquisition with the magnitude of the displacement in mm/s as shown in Figure 2.17. Here, the leftmost point is toward the tower, and the rightmost point is toward the shaker at midspan. The areas between measurement locations were automatically interpolated by the PSV software. The region near the center of the loop showed lower relative displacement, as expected for a node region. Similarly, the antinode regions at the ends of the loop showed high displacement.

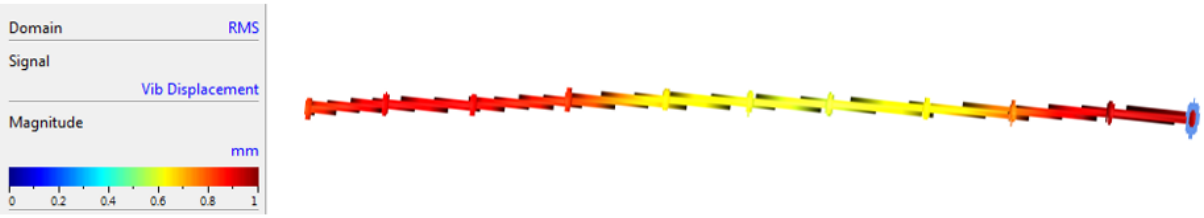

Figure 2.17: Displacement for the third loop of the cable without any mass attached.

When using stand-in masses for the robot, we found that the cable dynamics changed in accordance with our expectations, as shown in Figure 2.18. The displacement profile changed with the addition of a mass representing 15% ($383g$) of the cable mass. These results agree with our previous research on the effect of untuned masses, where we saw vibration loop lengths change in size with the addition of a mass [27]. The nature of these changes were based on the value of the mass and its position. There, we observed that the addition of a mass to the vibration loop caused the nodes to shift inward toward the antinode, which aligned with our numerical findings. Each increase in mass coincided with an increased shrinking effect.

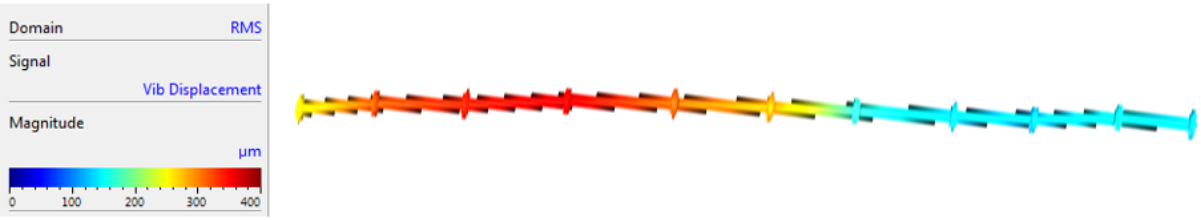

Figure 2.18: Displacement for the same cable segment with a mass corresponding to 15% of the cable mass attached at an antinode (A3).

The suspended masses were chosen to bring the total mass of the MDR to 5%, 15%, and 25% of the cable mass as given in Table 2.6. A maximum of 25% was used to prevent the introduction of undesirable static deflection.

Table 2.6: Masses Used for Testing

Target Percentage	**5%**	**15%**	**25%**
Target Mass	128g	384g	640g
Actual Mass	132g	383g	649g
Actual Percentage	5.16%	14.96%	25.35%
Percent Difference	3.13%	0.26%	1.41%

We documented a decrease in displacement across the cable with a lower maximum. By moving the scanning head further toward midspan, we found that the region of minimum displacement was enlarged compared to the cable without any mass attached, and that there was also an enlarged region of maximum displacement. These results were consistent for all three tested masses. One of the suspended masses used is shown in Figure 2.19.

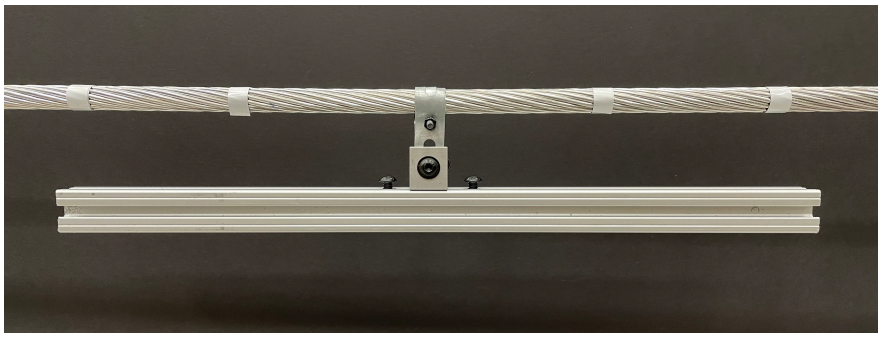

Figure 2.19: Mass suspended on the cable.

Additional investigations were performed with the 15% mass attached at both the theoretical node and antinode locations. Tests were performed for ten harmonics from the 3rd mode to the 12th mode. The first and second modes were excluded due to both the limitations of the shaker and the inaccessibility of node and antinode locations for mounting the mass. Eleven points were measured along the same section of cable for all of the tests. Figure 2.20a shows the results at the 4th mode, which most clearly demonstrated the effects of the suspended mass. Mounting the mass at an antinode location had a clear positive effect on vibration reduction. As expected, the introduction of the suspended mass also changed the locations of the antinodes due to its impact on the cable dynamics. As such, it was known prior to testing of the robot prototype that the robot would not be navigating to the theoretical antinode position but would adapt to the changes in the cable.

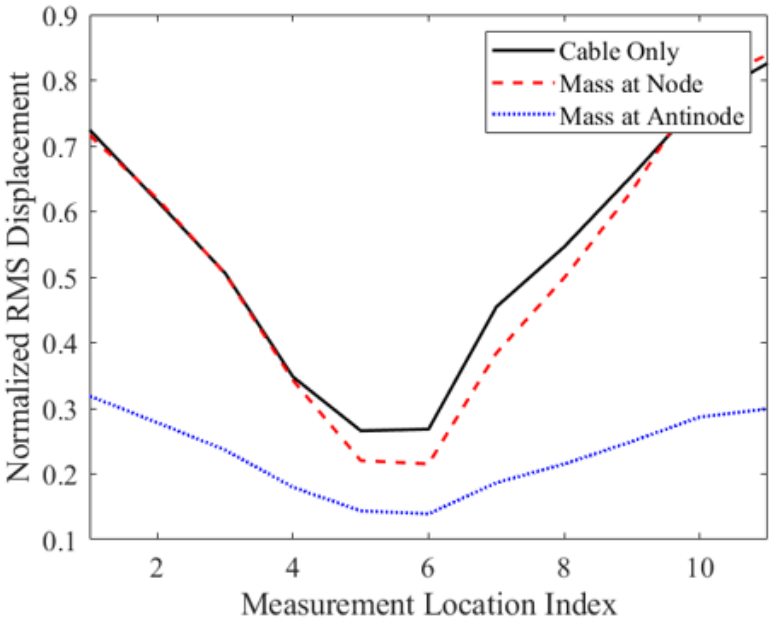

(a) Experimental normalized RMS displacement for the 4th mode at 16 Hz.

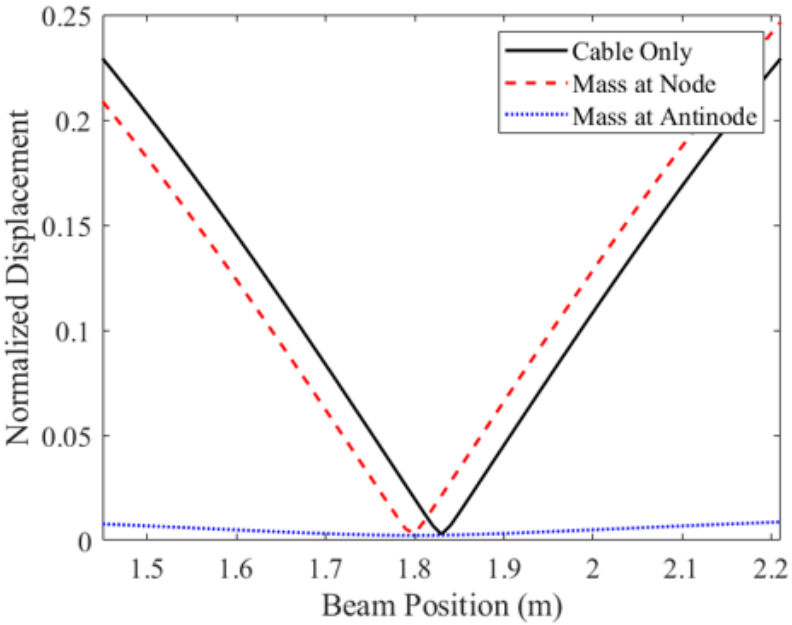

(b) Velocity for the 8th Mode.

Figure 2.20: Numerical normalized RMS displacement for the same location of the cable at the 4th mode.

These results were compared against the numerical results in MATLAB®, shown in Figure 2.20b. The ODE45 function was used to simulate the displacement of the cable and suspended mass. The magnitude of the displacement was normalized since the particular experimental values were dependent on the gain settings of the amplifier. The position is given in meters and aligns with the measurement location in Figure 2.20a. There is an overall agreement in general trends between the experimental and numerical results. Adding the mass at the position of an node did not significantly change the displacement from those of the cable alone. Conversely, adding the mass at the position of an antinode did significantly change the displacement to be well below the those of the cable alone. However, the fidelity of the model was limited by the use of the mode shapes for the bare conductor. Even so, these results were notably better than those found on the previous test bench despite using the same mathematical model. Evaluation of a string model was also performed, to worse results.

Figure 2.21 shows a comparison of the acceleration trends when the masses were placed at the nodes and antinodes. There is a clear contrast in agreement of results from the original test bench to the updated one. The original test bench saw a mismatch between the experimental and numerical results for the mass at the node. With the updated test bench, we saw agreements for this case, as well as with the mass at the antinode. These results indicated that the improved test bench was better suited for experiments, as it better aligned with the Euler-Bernoulli beam model. This was an important finding, as that mathematical model presented earlier in Section 2.1 has been well established in the literature for transmission lines commonly used in industry.

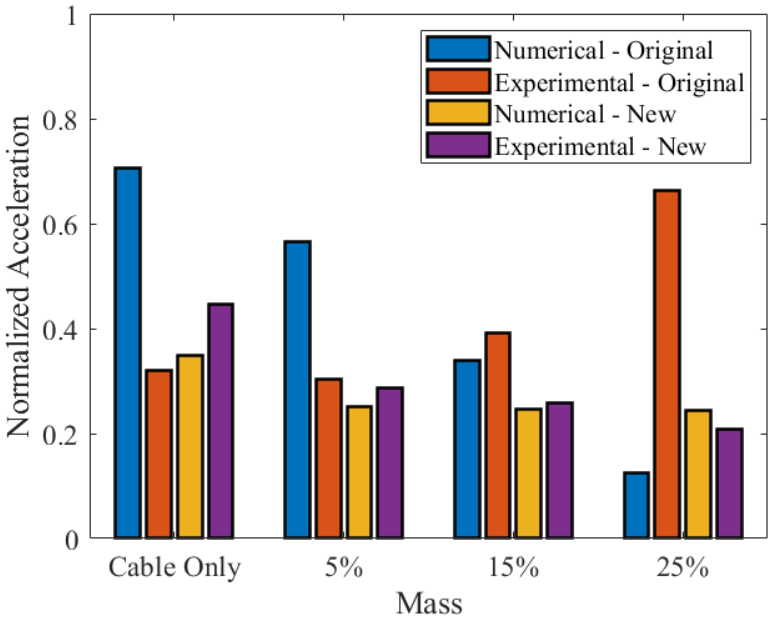

(a) Normalized acceleration with the masses suspended at the node.

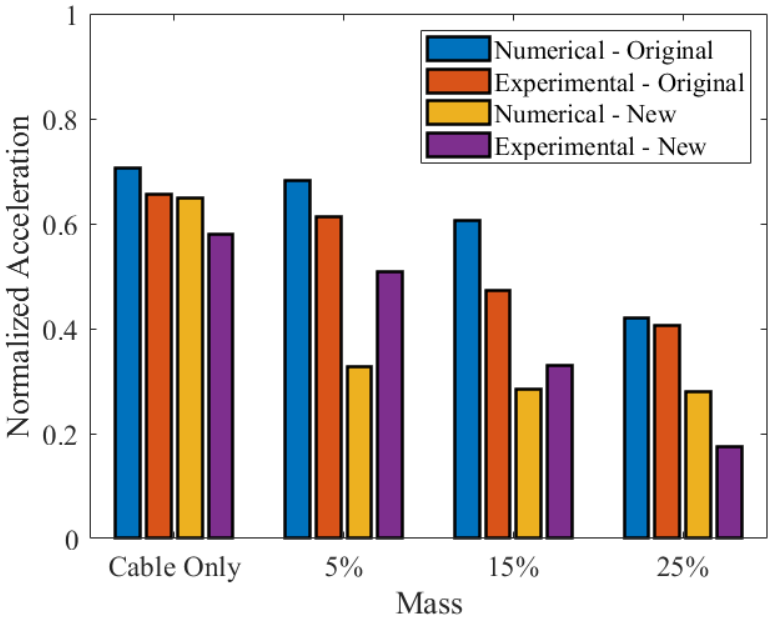

(b) Normalized acceleration with the masses suspended at the antinode.

Figure 2.21: Comparison of the acceleration trends between test benches.

2.4 Chapter Summary

This chapter discussed our success in establishing a suitable experimental test bench. Since we found that the original test bench did not match the well established mathematical model for transmission line conductors, we redesigned a completely new experimental setup. This setup was validated using the same mathematical model. As a result, we could have greater confidence that our experimental findings would translate to real world applications.

Chapter 3

Design and Development of an MDR Prototype

This chapter discusses the development of a small-scale MDR prototype for testing. We worked through several different designs with different focuses (repurposing parts, actualizing the conceptual design, and minimizing mass) before selecting a design that balanced our priorities. The final MDR prototype was well suited for the test bench and was devised to seamlessly integrate additional capabilities for future work.

3.1 Interim Prototypes

3.1.1 Rehoused Senior Design Robot

We initially considered rehousing some of the components used in the MDR prototype created for senior design. We had already established a clamping mechanism using Actuonix linear servos, validated that the motor's torque output was strong enough to drive the robot along the cable, and written code for all of the electronics used. A simplified version of the proposed design, with some exclusions, is shown below in Figure 3.1.

The chassis was to be constructed with Actobotics plates for easy changes during prototyping and testing, especially with the need to substitute some internal components. The dimensions

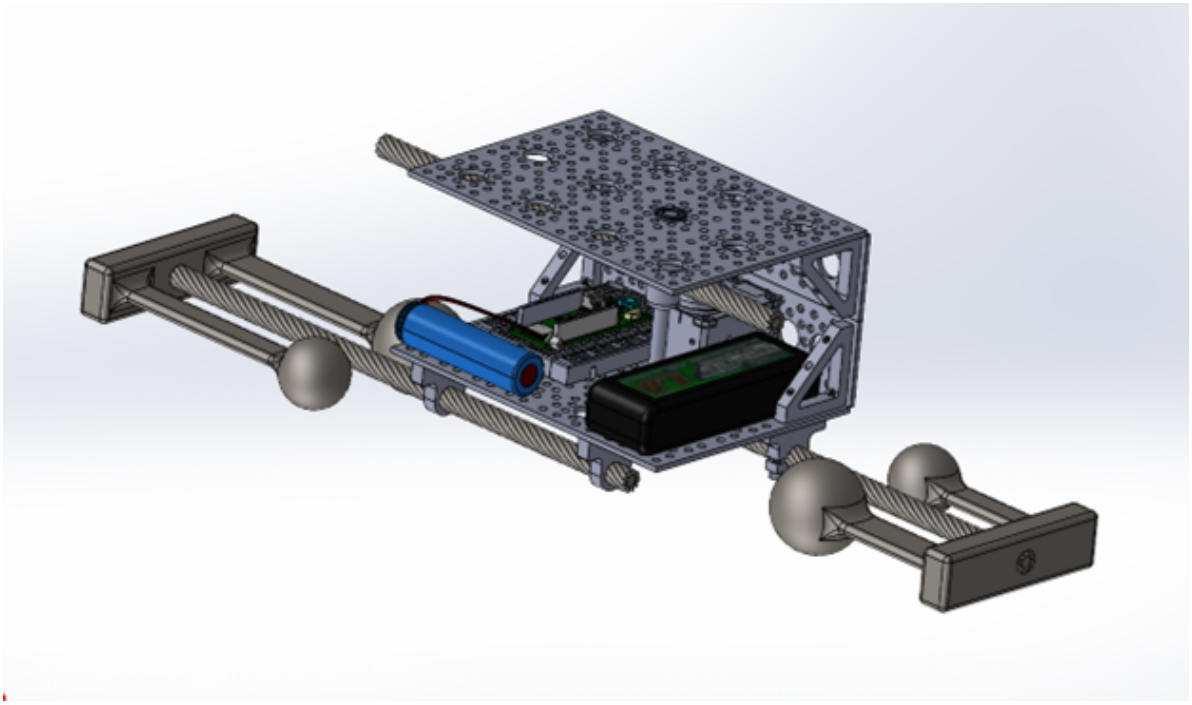

Figure 3.1: MDR prototype concept repurposing components from senior design. The side panel intentionally left suppressed from view.

were 15 cm (L) x 11.25 cm (W) x 7.5 cm (H), but could easily be altered to reflect actual spacing needs. They could also be layered to improved strength and rigidity, if needed. The robot would be mounted to the cable with two passive rollers on top and a single drive wheel underneath in a "V" configuration. It would have been impossible to repurpose the dampers fashioned for the much larger senior design robot, so the dampers designed by Barry et al [20] would be manufactured by a local machine shop. The dampers would be connected to the robot body via the use of clamping hubs that matched the hole pattern on the chassis plates.

However, this prototype design was quickly scrapped for several reasons. First, the clamping mechanism was not needed for the testing we were performing. Second, we wanted to transition to different motors. Third, this design would making mounting and dismounting the robot more difficult.

3.1.2 Pre-existing Conceptual Design

We next looked at a design for the MDR that had previously been conceptualized but required several changes for use with our experimental test setup. The original detailed design is depicted in Figure 3.2 based on the conceptual design shown in Figure 1.7 in Section 1.3. Firstly, the design needed to be largely simplified, as it had been imagined as a fully developed prototype for use on heavy duty conductors commonly used in industry. Since the first stage prototype was primarily for a proof-of-concept demonstration of the antinode tracking ability rather than full scale implementation, it was better to start from a simpler case. Therefore, we chose to change the damper design and attachments, reduce the framing, and remove the shell. Similarly, we also excluded from our scope energy harvesting, waterproofing, EM shielding, and heat dissipation.

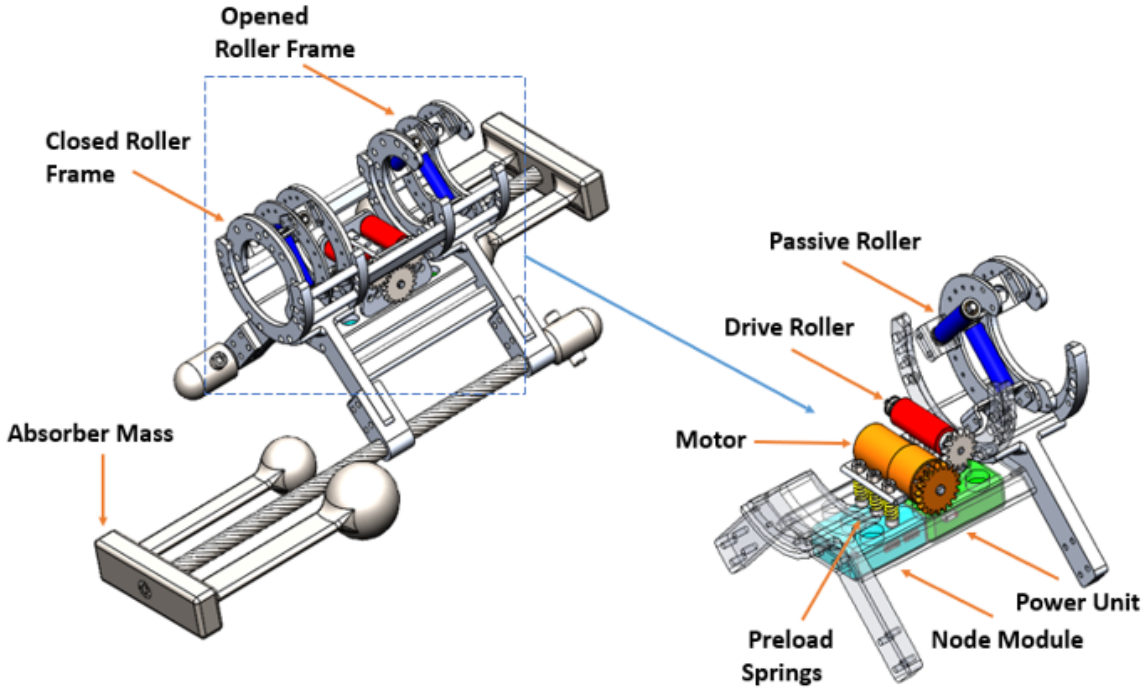

Figure 3.2: Original conceptual design of the MDR prototype.

Secondly, and in conjunction with simplification, we needed to reduce the weight of the robot. Since a large robot would increase static deflection and have a greater impact on cable dynamics, we sought to minimize the weight as much as possible, especially since our original test cable weighed less than a kilogram. The primary changes would be to fabricate using 3D printed PLA (polyactide) instead of metal, reduce the size of the robot, and use a simplified single damper mounted directly to the bottom plate of the frame.

Lastly, we wanted to transition to Dyanmixel motors for their precision and native ability for PID control. However, their form factor was quite different from most motors, which required us to modify the motor module. Additionally, the surrounding components had to be shifted to accommodate the single damper design, which also meant changes to the motor module. This was due to the single damper lying directly below the center of mass of the robot rather than offset on the sides as seen in the conceptual design.

The modifications to the motor module became the focus of our work. We changed the spacing to accommodate the damper and reduce the chassis size. We switched from gears to belts since they were cheaper with better tolerance for misalignment. We used two motors for more torque and improved balance. We added a base plate for more secure mounting. We added hubs, brackets, and flanged bearings. And we switched to wave springs for more symmetrical force distribution. Figure 3.3 shows various stages of design and prototyping.

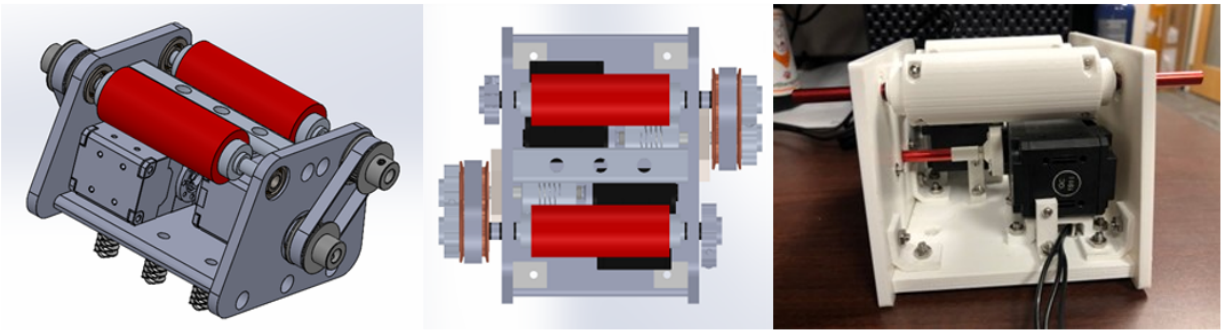

Figure 3.3: Development of the motor module.

Ultimately, it became apparent that retooling even a limited scope version of the original conceptual design was unnecessary and too time-consuming for our purposes. It would also be difficult to ensure the required rigidity while using 3D printed parts. Additionally, it was nearly impossible to design an appropriately lightweight version of this prototype. The motor module alone constituted a mass of several hundred grams, meaning a total in-span mass of over a kilogram. This would force us to use a much smaller suspended mass than intended and create an undesirable ratio of in-span mass to suspended mass [41, 42].

3.1.3 Ultra Lightweight

We then transitioned to an MDR prototype meant to be as simple and lightweight as possible, with a total mass of under 15% of the cable weight. As mentioned in Section 2.3.1, the cable was 2.56 kg. Therefore, we were limited to a maximum mass of around 384 g. Figure 3.4 shows different stages of design and prototyping. The chassis was eliminated and replaced with connecting frames. The batteries were removed, with the motors and microcontroller to instead be powered via DC power adapter and USB connection. The robot mass as shown was roughly 150 g, so the damper would have been almost 250 g, giving an in-span to suspended mass ratio of 3:5.

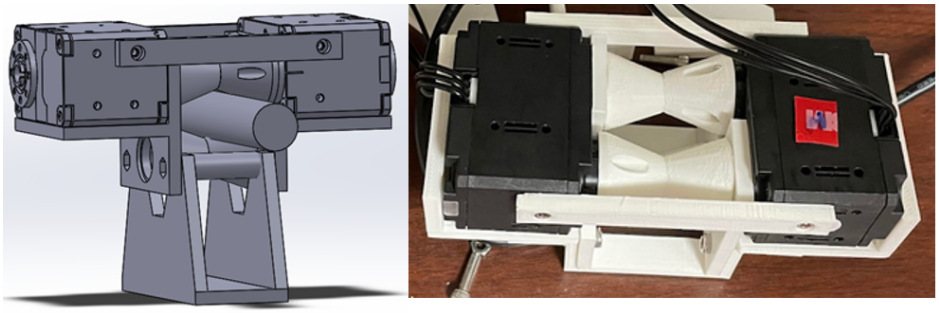

Figure 3.4: Development of the ultralight prototype. The carriage shown in the left hand CAD model was used for electronics and damper attachment.

This version was also discontinued, as it was difficult to mount and dismount and lacked balance. The latter was somewhat expected since the motors needed to be placed on either side of the cable to avoid a more complicated drive train. The motors could not be mounted underneath the cable due to both the poor tolerance of the 3D printed wheels and the irregularities in the cable that caused slippage during locomotion.

3.2 Final Prototype

3.2.1 Mechanical Design

We settled on a mid-scale prototype for the MDR, as shown in Figure 3.5. There were two key considerations for this test prototype: 1) Stability and 2) Mass. However, in this case, we chose to aim for closer to 25% of the cable mass to allow for more flexibility in our design. We also prioritized ease of mounting and dismounting.

To address the stability, we used two points of contact on the cable. This prevented undesirable sway and allowed the robot to stabilize more quickly after locomotion. The first contact was a set of drive wheels mounted vertically, preventing rotation about the cable axis. The second contact was a set of rollers mounted horizontally to prevent oscillation along the cable axis. The drive wheels and rollers were placed as close together as possible since we wanted to minimize the distance of either contact point from the antinode. We also designed the robot so the center of mass was along the mid-line of the robot longitudinally and as close to the center of the robot as possible. This would put it directly below the cable for better balance.

To address the mass, we designed the MDR to be as lightweight as feasible. The MDR has both an in-span mass and a suspended mass. As determined by Kakou et al [42], it is better

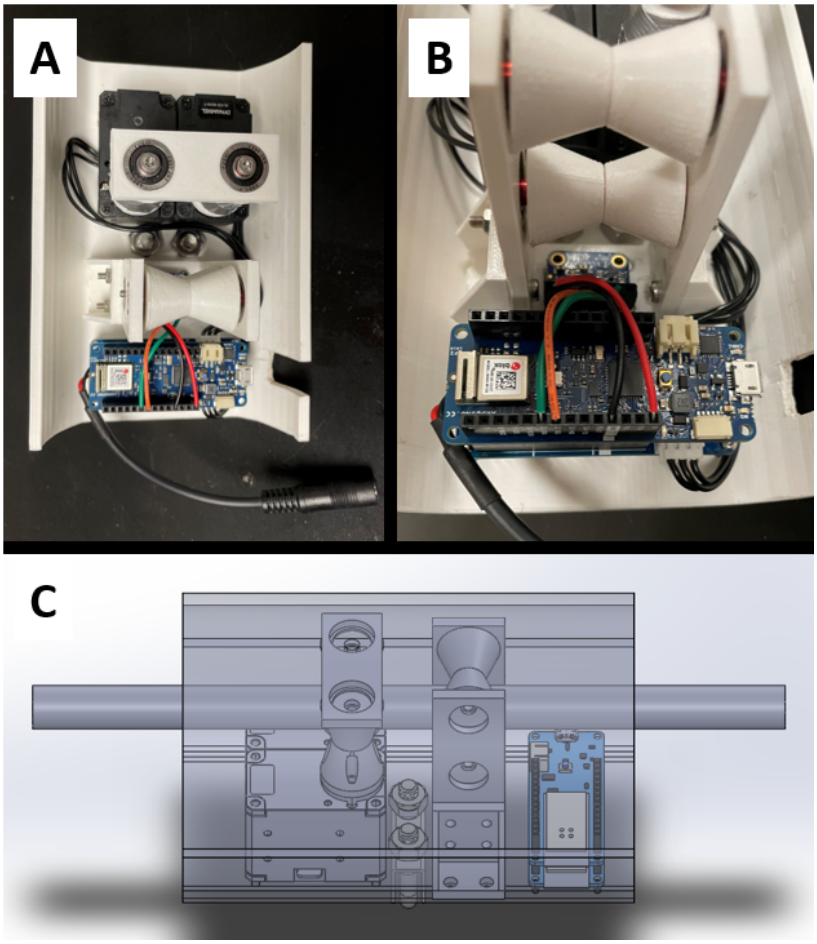

Figure 3.5: MDR test prototype. A) Top level view of the motors, drive wheels, rollers, and microcontroller. B) Front view of the rollers, accelerometer, and microcontroller. C) Side view of the CAD model.

is keep the in-span mass of the robot low to maintain a low ratio of in-span mass (robot components and hardware) to suspended mass (absorber). This was particularly important due to the relatively low mass of the cable at just 2.56 kg. As previously mentioned, a total mass of greater than 25% of the cable mass is undesirable due to the static deflection this introduces to the cable, as well as the additional strain this would contribute to the conductor in real world conditions. For this reason, we continued to exclude components such as the clamp and battery pack. A removable top shell was also left unattached during testing since it reduced the robot weight by 64 g.

As Dynamixel servos are primarily used to articulate joints, we had to design a custom hub and drive wheels. The rollers were attached to the bearings using threaded standoffs and screws as the axles. All parts were constructed using 3D printed PLA (polyactide) components and off-the-shelf hardware. The damper was a stainless steel rod mounted to the bottom of the robot body using a U-clamp. The rod was selected to have a high mass while being close to 25% of the cable mass (640 g). The dimensions of the final MDR prototype are defined in Table 3.1.

Table 3.1: MDR Prototype Dimensions

Dimension	**Value**
In-Span Mass	404 g
Suspended Mass	281 g
Length	15 cm
Width	10 cm
Height	8 cm

3.2.2 Electronics

The robot is driven by two Dynamixel XL430-W250-T servo motors with 360° continuous rotation capability. At just 57.2 g, each motor has a stall torque of 1.4 Nm at 11.1 V and 1.3 A. The XL 430 has an onboard MCU that utilizes PID control and an integrated absolute rotary encoder for feedback of the shaft position. The motor also comes equipped with various control profiles such as Velocity Control Mode, which is ideal for wheel operation. An additional advantage of Dynamixel servos is the ability to use a common bus for multiple servos with each assigned a unique ID. Since two drive wheels were necessary for more stable and reliable operation, we were able to use both servos without the need for additional motor drivers or the use of dedicated PWM pins.

An Arduino MKR 1010 microcontroller was used. The primary reasons for choosing this microcontroller were the simplicity of programming and the widespread availability of compatible peripheral components, such as the Dynamixel shield to interface with the motors. While a shield was also available for the Arduino Uno, the Uno has a larger form factor and lacked the RF, WiFi, and Bluetooth capabilities of the MKR. Although early stage testing did not require wireless communication, it will be necessary at the next stage when the robot is battery powered and self-contained. Therefore, it was better to design from the beginning with respect to the proper microcontroller.

The Adafruit MMA8451 accelerometer was used for its ease of use and low cost. It comes pre-calibrated and has a high maximum sample rate of 800 Hz with a range of up to 8 Gs. The accelerometer can also output orientation data. The robot was powered using a DC power supply into the Dynamixel Shield for the motors and via USB for the Arduino. This reduced weight and gave access to the Serial Monitor.

3.3 Antinode Tracking Algorithm

Control algorithms relevant to antinode tracking have been lacking in the literature due to the novelty of the MDR. While other power line inspection robots have been developed, they have key design differences that prevent their controls from being utilized in the MDR. For example, many robots are designed to simply travel continuously along the cable, they are designed to overcome obstacles, and they have articulating limbs. Consequently, research has been more focused on aspects such as mapping and path planning, controlling the robot center of mass, and joint kinematics.

The goal of the algorithm tracking algorithm is to autonomously navigate the robot to the antinodes of the cable without knowledge of cable parameters or user input. To achieve

this goal, we implemented an iterative improvement local search algorithm. A single root mean square acceleration (G_{RMS}) value is saved at any given time, and the robot acts to improve the value with each iteration until it finds the highest value. The RMS value was used rather than peak or peak-to-peak amplitude since it is directly related to the energy of the vibration. A high level overview of the control algorithm is depicted in Figure 3.6.

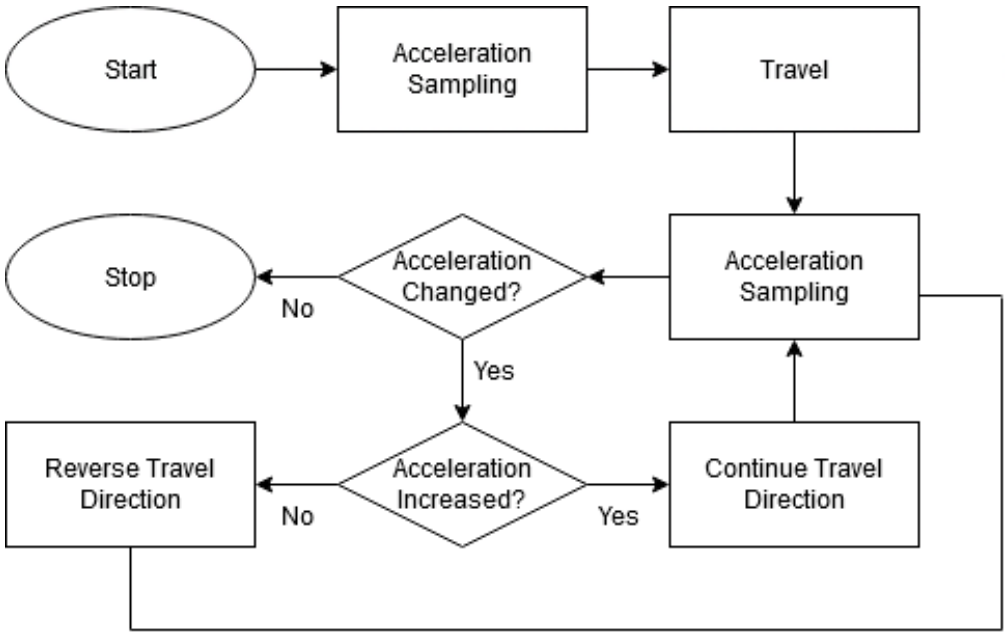

Figure 3.6: Overview of Antinode Tracking Algorithm.

A sample set of acceleration values is recorded in an array, and the G_{RMS} is calculated. Then, the robot moves a predefined distance, whereupon it takes another sample. The G_{RMS} of the new sample is compared to the G_{RMS} of the previous sample. If the acceleration has increased, the robot will continue in the same direction. If the acceleration has decreased, the robot will reverse direction. The robot continues this cycle of sample, travel, compare until it reaches a position where the acceleration has not changed significantly from the previous position, indicating the successful navigation of the robot to the location of the antinode.

The significance of the acceleration change is determined by a set threshold of the previous G_{RMS} value +/- a margin. To prevent unnecessary oscillation, several safeguards were put

into place. First, the robot was programmed to take a large number of samples at each location at an appropriately high sample rate to prevent aliasing and ensure an accurate G_{RMS} value at each location. A delay was implemented after locomotion before taking a new sample to allow the transient response to settle. The robot was programmed to take larger steps than necessary to ensure significant differences in acceleration values between locations. Lastly, the margin was tuned to the amplitude of the excitation and based on the tolerance of the accelerometer and amplifier gain.

3.4 Chapter Summary

This chapter discussed the design process to develop the prototype of the MDR for testing. We outlined the progression of potential prototypes and why each was rejected. Then we reviewed the reasoning for the final version, including the mechanical design, electronics used, and how the antinode tracking algorithm works.

Chapter 4

Successful Demonstration of Autonomous Navigation

This chapter details how the antinode tracking algorithm was validated with the MDR prototype on the test bench. We mapped the displacement of the cable along the cable region used for testing. We manually moved the robot along the cable and assessed the acceleration trends. Then we experimentally demonstrated the ability of the MDR to travel to the locations of highest amplitude. Finally, we proposed an alternative algorithm that may boost performance.

4.1 Testing & Validation

As with the validation of the test bench in Section 2.3.3, we chose to perform the algorithm testing at the 8th harmonic of the cable, or 32 Hz. Loops 2 and 3 were again used for testing as well. An image of the MDR prototype on the cable during testing is shown in Figure 4.1. Although we knew where the antinodes were along the cable from the PSV vibrometer and via visual confirmation of the theoretical locations, these were for the conductor alone. Once the MDR was placed on the cable, the altered dynamics would mean we no longer knew where the antinodes were located, especially as the robot moved. As such, we needed to first determine where the cable antinodes were with the robot on the cable.

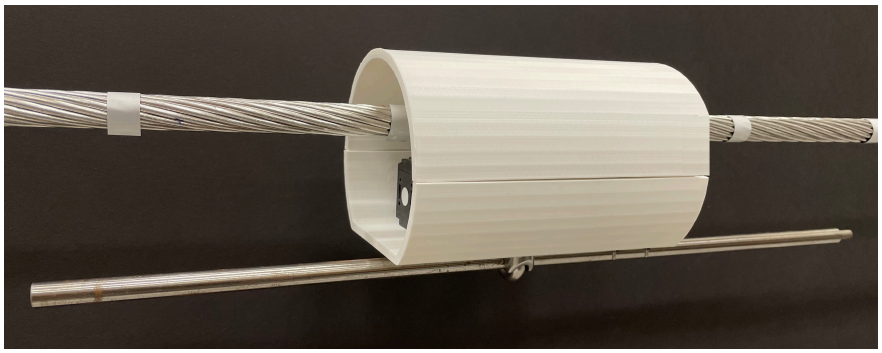

Figure 4.1: MDR Prototype mounted on the test cable. The top shell was removed during testing.

Since it was not feasible to solve for all these changes analytically or capture all of them with the vibrometer, it was necessary to map the relative displacement along the test section of the cable with the MDR. To accomplish this, we created a simple program to continuously sample the acceleration at a uniform rate of 200 Hz as the MDR slowly traveled along the cable at a slow pace of roughly 0.5 m/min. The acceleration data was filtered by a bandpass filter, then the displacement was estimated by dividing the filtered data by $(2\pi f)^2$. The displacement was also calculated by integrating the filtered acceleration data twice in the frequency domain. Figure 4.2 shows plots of both sets of normalized data.

This procedure was repeated with the PCB Piezotronics 352C33 accelerometer sampling at 256 Hz for comparison. Both plots are given below in Figure 4.3. The results between both pairs of displacement plots showed good agreement, and several antinode locations can clearly be seen. These locations were marked on the cable. Interestingly, while the antinodes did appear to move away from the middle of the vibration loops, the locations of nodes did not seem to change. Although this may seem contrary to previous experiments that showed the node moved inward, this is explained by those previous measurements being done relative to the mass at the theoretical antinode position. In this case, the measurements are taken at the same location as the MDR.

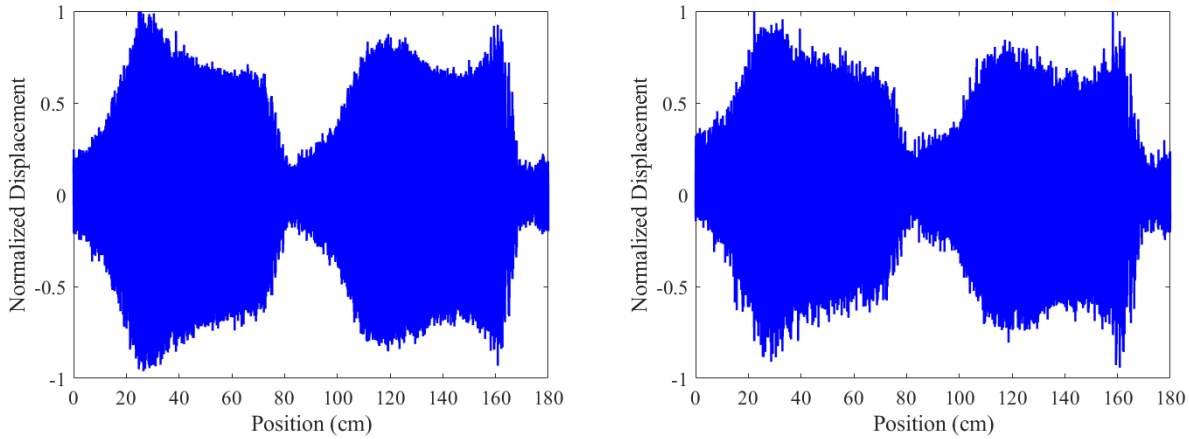

(a) Estimated displacement using data from the onboard accelerometer.

(b) Integrated displacement using data from the onboard accelerometer.

Figure 4.2: Comparison plots of normalized displacement as the robot traveled along the cable between N2 to N4 (Loops 2 & 3).

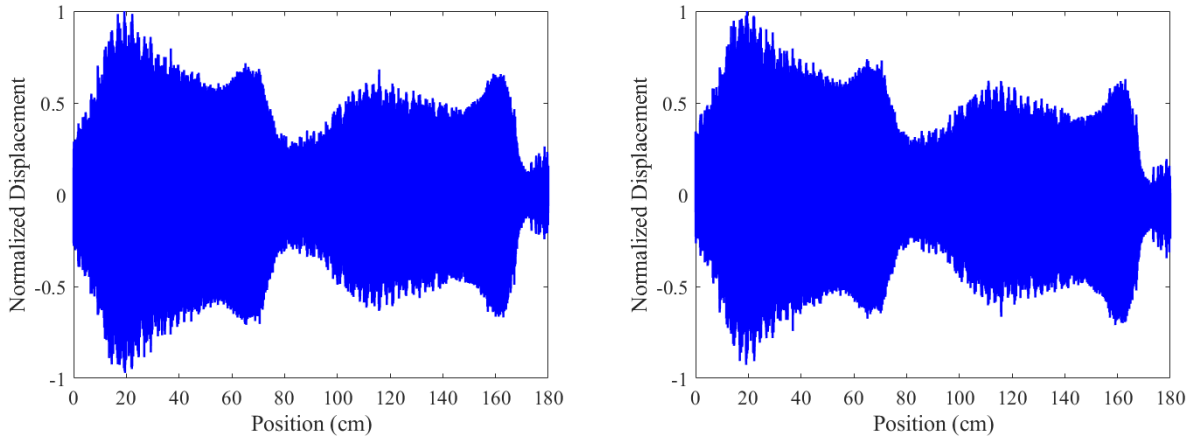

(a) Estimated displacement using data from the piezoelectric accelerometer.

(b) Integrated displacement using data from the piezoelectric accelerometer.

Figure 4.3: Comparison plots of normalized displacement as the robot traveled along the cable between N2 to N4 (Loops 2 & 3).

Figure 4.4 shows the peak, peak-to-peak, and RMS accelerations at 22 points along the two vibration loops of the test region. The robot was manually moved in 8.75 cm increments since this was the travel step distance between samples. The values shown here overall align with the trends seen in Figure 4.2.

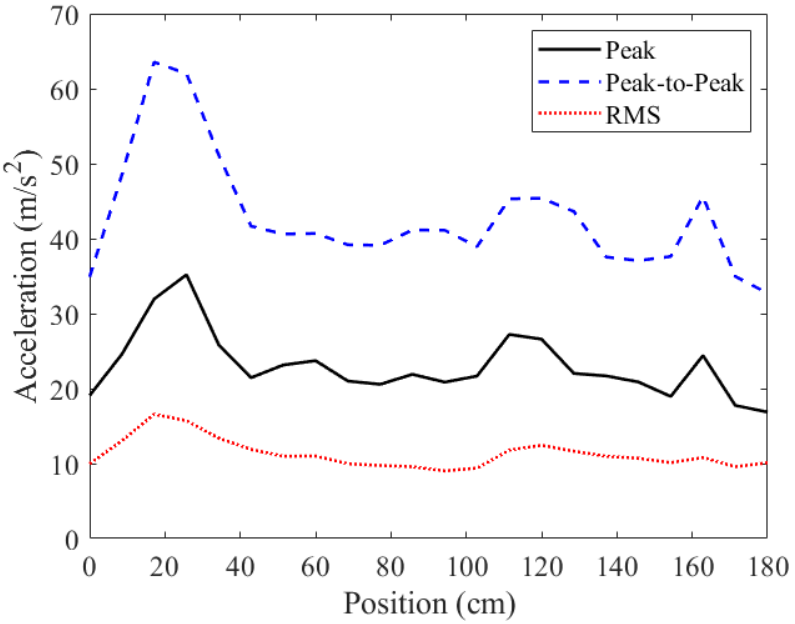

Figure 4.4: Acceleration of the system with the robot mounted at various points along the testing region.

The antinode tracking algorithm was tested with the MDR mounted at multiple locations along the test region for multiple trials at each location. The performance was judged based on the MDR's ability to consistently travel to the marked antinode position along the cable. Variables such as the margin, step distance, and delay were adjusted based on the robot's performance.

4.2 Results

Early testing of the algorithm showed modest success, but several issues arose. For example, it took the MDR quite a bit of time to get to the antinode position because it stalled at several locations and tended to oscillate about these locations before eventually moving on from these "false antinodes." To fix this, we increased the travel distance between testing locations multiple times up to 8.75 cm, which ultimately worked well. This caused there to

be a more distinct change between locations to reliably reach the threshold value. We also increased the delay time before taking samples at a new location to two seconds to better avoid any transient response from the robot's movement from confounding the results. We tested increasing the number of samples above 200, but found no difference in the results.

Once these changes were made, the MDR's performance improved significantly, and the robot was able to reliably navigate to the marked antinode locations each time when placed at various points along the testing region. Figure 4.5 depicts the view from the vibrometer of the cable, with the acceleration values for each measurement location on the cable. Locally, the MDR suppressed the vibration to well below the acceleration on either side of its position. Despite the high acceleration to the right of the MDR position, the MDR was actually at the best location for damping vibration. When adjusted to sit at the location of the red measurement, the acceleration simply shifted along the cable with no reduction in magnitude.

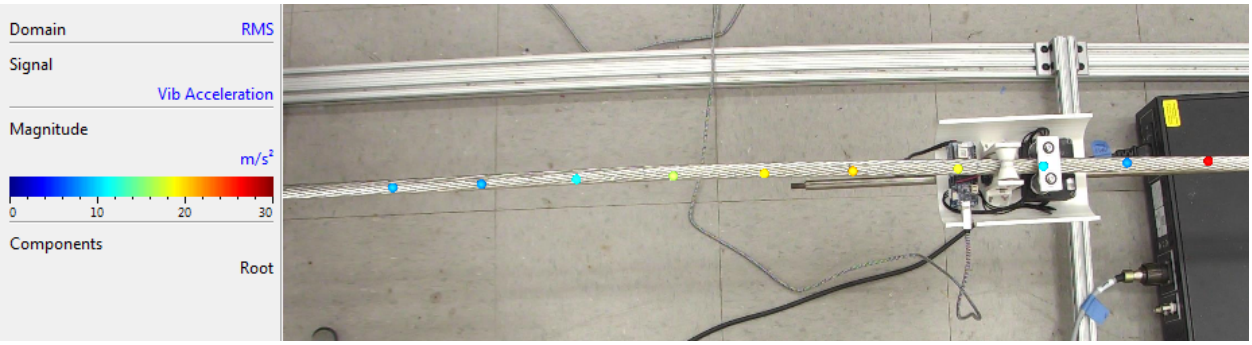

Figure 4.5: Acceleration of the vibration loop with the MDR at the location of the antinode. Adjusting the robot toward the higher acceleration location to the right shifted but failed to reduce the acceleration along the cable.

Additional testing was performed at 36 Hz (9th mode shape), again for Loops 2 and 3. This did not impact the ability of the robot to navigate to the locations of highest acceleration magnitude as verified by the scanning head. Additional tests were also performed with different gains, and the MDR prototype was again able to navigate to the antinode locations once the margin for the threshold value was appropriately tuned.

The accuracy of the robot to the antinode is theoretically within half the predefined travel distance between sample locations due to the antinode lying within the two contact points of the MDR. For an 8.75 cm travel distance and a loop length of 0.92 m, this represents a positional accuracy of 4.8%. The accuracy could potentially be further increased by decreasing the travel distance, but this may result in an inability to reach the antinode if the acceleration at adjacent locations is too similar and the threshold is not reached.

We also explored comparison testing with peak amplitude by finding the maximum of the absolute values of the sample sets. We performed limited testing with peak-to-peak amplitude as well. As expected, the implementation of the algorithm using G_{RMS} performed better than these alternative versions, which resulted in less direct paths to the antinodes with far more oscillation. They also struggled to find the antinode at higher gains even when the margin was tuned.

Another variation of antinode tracking we are currently exploring is a method of navigation where the MDR simply traverses a proscribed length of the cable to map the acceleration in that region. This could be accomplished via an iterative movement approach. The MDR would move to each measurement location and find the G_{RMS} as with the original program. However, it would now store it in an array where each acceleration value is indexed according to the number of travel steps. Then once the MDR has finished traveling across the region, it would find the maximum G_{RMS} value of all indices, then travel back to that location. For example, if the robot needed to check a region of a meter, it could travel in 5 cm increments with each increment indexed 1-20. If it found that index 6 had the highest acceleration, then it would travel back 14 travel steps (20 - 6) to get to the best antinode location. The MDR would also verify that it was at the correct location by sampling again and comparing against the values it acquired earlier. The benefit of such a navigation program would more reliable navigation to the global maximum of that region while avoiding oscillation about

antinode locations. The drawback would be the increased energy expenditure. A difficulty would be setting the travel region, but this could be configured based on loop length sizes determined via a parameterization study for common ranges of cable diameter and length.

4.3 Chapter Summary

This chapter discussed the validation process of the antinode tracking algorithm. The MDR was consistently able to navigate to the antinode locations of the cable under various excitation conditions. This successful demonstration allows us to move forward in the MDR's design and incorporate additional capabilities.

Chapter 5

Conclusion & Future Work

5.1 Conclusion

In this thesis, we highlighted the need for the MDR to fill a gap in current methodologies for overhead transmission line vibration mitigation and inspection. We reviewed the evolution of a suitable experimental test bench that matched our mathematical model. We reviewed the process of designing and prototyping the MDR. And we validated the ability of our antinode tracking algorithm to navigate the MDR to the antinodes of the cable without a priori knowledge of cable parameters. This research directly contributes to the MDR's development by progressing the technology, thereby making a full-scale prototype more achievable.

We defined a mathematical model of the system and used it to invalidate the pre-existing experimental test bench. We then designed and constructed an improved test setup. The analytical and numerical analyses demonstrated that a beam model is more appropriate than a string model. Moreover, the new test bench produced good agreement in trends between the numerical and experimental results. This further indicated that the new test bench adequately adhered to the Euler-Bernoulli beam model that best captures the dynamics of conductors used in industry today. Therefore, we could better assume that the results of experiments carried out on the new setup would better translate to real world conditions. As such, the insights gained from testing could be generalizable to broader use, thereby guiding the MDR's continued development. The test bench was also designed to be modular, so

additional testing under different conditions can also be done.

We designed and constructed several test prototypes for the MDR. Early versions suffered from a number of drawbacks that made their continued development impractical. We settled on a simplified prototype with a mass roughly equal to 25% of the cable mass. To autonomously navigate the robot to the antinodes of the cable, we developed an antinode tracking algorithm that used iterative improvement to find the local maximum acceleration. The testing of the MDR prototype on the cable demonstrated that the robot was able to navigate to the regions of highest amplitude corresponding to the antinode under various excitation conditions. These results indicated that the antinode algorithm can effectively track the vibration antinodes as desired. We also found that the MDR helped reduce the average vibration of the system for different resonance frequencies, even while transporting untuned vibration absorbers. This is consistent with previous results and suggests that the MDR should have a positive impact on conductor vibration even when the suspended vibration absorber is not tuned to a given resonance frequency of the conductor. This is especially important given the limited resonance frequencies that a single vibration absorber can address.

5.2 Future Work

To further improve the MDR's performance, we will assess the cable response with tuned absorbers. We attempted to tune the damper mass by iteratively adding additional masses to the ends. However, the stiffness of the damper mass (stainless steel rod) was far too high, resulting is a high first mode. We were unable to decrease the first mode without using excessively large weights that would increase the MDR's mass to well above 25% of the cable. A less rigid material such as aluminum could be used. Or the damper could be

modeled and tuned via simulation with computer-aided design software.

We will also adjust the placement of the electrodynamic shaker and perform testing of the robot at various points along the cable while excitation conditions change. This is necessary to ensure that the robot can adapt to the changes in wind conditions in real-time. Although the placement of the shaker away from mid-span has been shown by previous testing to produce more unequal loop lengths, it would be interesting to see what effect, if any, this has on the MDR's performance.

We will make several improvements to the antinode tracking algorithm. In addition to testing the new navigation method proposed in Section 4.2, we can revise the algorithm to be more adaptive and robust. Boundary setting would prevent the robot from running into a tower. It could also be used to keep the robot closer to the tower, since this would reduce strain on the conductor. Dynamic parameter setting would allow the robot to set the margin, travel distance, and other parameters automatically based on the magnitude of the acceleration sample sets. An additional accelerometer should be incorporated onto the damper of the robot to explore how transmissibility varies along the conductor. This would be another input into the antinode tracking algorithm to ensure the MDR reaches the antinode.

Furthermore, testing will be performed with a longer, larger diameter cable, possibly with steel reinforcement to further increase the dominance of the EI term for even better adherence to the beam model. The increased mass of the cable would also accommodate a heavier MDR prototype that can incorporate the clamping mechanism, a better drive train, and additional sensors. The motors will be powered by an 11.1V lithium ion battery pack, as recommended by the manufacturer. The Arduino MKR will have its own dedicated power source of a 3.7V 18650 battery with JST connector. Without the USB connection to the Serial Monitor, the Arduino MKR's wireless data transmission capabilities should be utilized. The additional sensors can be used to incorporate inspection capabilities and test

these operations. For example, images from an inspection camera could be transmitted.

Eventually, a more extensive prototype should be developed for use in industrial testing. For example, the chassis should be metal to increase rigidity, and the wheels should be made of a better material such as Nylon with springs for pretension to ensure secure mounting and reduce slippage. This could also be designed to accommodate cables of various diameters. Additionally, a secure clamping mechanism should be added back in to reduce internal disturbances that add noise to the accelerometer readings. The electronics should also be upgraded. A Teensy MCU can be used for control with an OpenCM module for the motors, and a Zigbee could be used for communication. An accelerometer with a higher sample rate and six degrees of freedom (triple axis accelerometer and triple axis gyroscope) could be used. A magnetometer will not be necessary, as it will likely not be useful on a live conductor. Testing should also be performed in a wind tunnel with an accompanying change to the model to simulate a uniformly distributed wind force composed of various frequencies. As the MDR develops, there should also be considerations for energy-harvesting to recharge the batteries so that the robot can be self-contained.

Bibliography

[1] Allied Market Research. Inspection robots market, Aug 2021. https://www.alliedmarketresearch.com/inspection-robots-market-A08254, Accessed on 2022-09-18.

[2] Randa Almadhoun, Tarek Taha, Lakmal Seneviratne, Jorge Dias, and Guowei Cai. A survey on inspecting structures using robotic systems. *International Journal of Advanced Robotic Systems*, 13(6):1729881416663664, 2016.

[3] American Society of Civil Engineers. 2021 infrastructure report card, March 2021. https://infrastructurereportcard.org/wp-content/uploads/2020/12/Energy-2021.pdf, Accessed on 2022-09-18.

[4] Andlinger Center for Energy and the Environment. Big but affordable effort needed for america to reach net-zero emissions by 2050, princeton study shows, December 2020. https://www.princeton.edu/news/2020/12/15/big-affordable-effort-needed-america-reach-net-zero-emissions-2050-princeton-study, Accessed on 2022-09-18.

[5] Ansys. Beam188 element, Mar 2017. https://www.mm.bme.hu/~gyebro/files/ans_help_v182/ans_elem/Hlp_E_BEAM188.html, Accessed on 2023-01-10.

[6] Nilson Barbieri, Oswaldo Honorato de Souza Júnior, and Renato Barbieri. Dynamical analysis of transmission line cables. part 1—linear theory. *Mechanical Systems and Signal Processing*, 18(3):659–669, 2004.

[7] O Barry, DCD Oguamanam, and DC Lin. Free vibration analysis of a single con-

ductor with a stockbridge damper. In *23rd Canadian Congress of Applied Mechanics (CANCAM 2011)*, pages 5–9. Vancouver Canada, 2011.

[8] O Barry, DCD Oguamanam, and JW Zu. On the dynamic analysis of a beam carrying multiple mass-spring-mass-damper system. *Shock and Vibration*, 2014, 2014.

[9] O Barry, JW Zu, and DCD Oguamanam. Forced vibration of overhead transmission line: analytical and experimental investigation. *Journal of Vibration and Acoustics*, 136 (4), 2014.

[10] O Barry, JW Zu, and DCD Oguamanam. Analytical and experimental investigation of overhead transmission line vibration. *Journal of Vibration and Control*, 21(14):2825–2837, 2015.

[11] O Barry, R Long, and DCD Oguamanam. Rational damping arrangement design for transmission lines vibrations: analytical and experimental analysis. *Journal of Dynamic Systems, Measurement, and Control*, 139(5):051012, 2017.

[12] O Barry, R Long, and DCD Oguamanam. Simplified vibration model and analysis of a single-conductor transmission line with dampers. *Proceedings of the Institution of Mechanical Engineers, Part C: Journal of Mechanical Engineering Science*, 231(22): 4150–4162, 2017.

[13] OR Barry, Y Zhu, JW Zu, and DCD Oguamanam. Free vibration analysis of a beam under axial load carrying a mass-spring-mass. In *International Design Engineering Technical Conferences and Computers and Information in Engineering Conference*, volume 45004, pages 791–796. American Society of Mechanical Engineers, 2012.

[14] OR Barry, DCD Oguamanam, and JW Zu. Nonlinear vibration of an axially loaded

beam carrying multiple mass–spring–damper systems. *Nonlinear Dynamics*, 77:1597–1608, 2014.

[15] Oumar Barry. Finite element analysis of a single conductor with a stockbridge damper under aeolian vibration'. *MASc, Mechanical Engineering, Ryerson University, Toronto, Canada*, 2010.

[16] Oumar Barry and Mohammad Bukhari. On the modeling and analysis of an energy harvester moving vibration absorber for power lines. In *Dynamic Systems and Control Conference*, volume 58288, page V002T23A005. American Society of Mechanical Engineers, 2017.

[17] Oumar Barry, Donatus CD Oguamanam, and Der Chyan Lin. Aeolian vibration of a single conductor with a stockbridge damper. *Proceedings of the Institution of Mechanical Engineers, Part C: Journal of Mechanical Engineering Science*, 227(5):935–945, 2013.

[18] Oumar Barry, JW Zu, and DCD Oguamanam. Nonlinear dynamics of stockbridge dampers. *Journal of Dynamic Systems, Measurement, and Control*, 137(6):061017, 2015.

[19] Oumar Rafiou Barry, Emadeddin Y Tanbour, Nitish Kumar Vaja, and Hesham Tanbour. Asymmetric aeolian vibration damper, April 17 2018. US Patent 9,948,081.

[20] Oumar Rafiou Barry, Emadeddin Y Tanbour, Nitish Kumar Vaja, and Hesham Tanbour. Asymmetric aeolian vibration damper, April 17 2018. US Patent 9,948,081.

[21] Rafiou Oumar Barry. *Vibration Modeling and Analysis of a Single Conductor With Stockbridge Dampers*. PhD thesis, University of Toronto, 2014.

[22] GE Braga, R Nakamura, and TA Furtado. Aeolian vibration of overhead transmission line cables: endurance limits. In *2004 IEEE/PES Transmision and Distribution Confer-*

ence and Exposition: Latin America (IEEE Cat. No. 04EX956), pages 487–492. IEEE, 2004.

[23] Mohammad A Bukhari and Oumar R Barry. Nonlinear vibrations of a beam-spring-large mass system. In *ASME International Mechanical Engineering Congress and Exposition*, volume 58387, page V04BT05A061. American Society of Mechanical Engineers, 2017.

[24] Mohammad A Bukhari and Oumar R Barry. Nonlinear vibrations analysis of overhead power lines: A beam with mass–spring–damper–mass systems. *Journal of Vibration and Acoustics*, 140(3), 2018.

[25] California Department of Forestry and Fire Protection. Cal fire investigators determine cause of the camp fire, May 2019. `https://www.fire.ca.gov/media/5121/campfire_cause.pdf`, Accessed on 2022-09-18.

[26] Kyeong Ho Cho, Young Hoon Jin, Ho Moon Kim, Hyungpil Moon, Ja Choon Koo, and Hyouk Ryeol Choi. Multifunctional robotic crawler for inspection of suspension bridge hanger cables: Mechanism design and performance validation. *IEEE/ASME Transactions on Mechatronics*, 22(1):236–246, 2016.

[27] Andrew Choi, Paul-Camille Kakou, and Oumar Barry. Considerations for the testing and validation of a mobile damping robot for overhead power lines. In *International Design Engineering Technical Conferences and Computers and Information in Engineering Conference*, volume 86311, page V010T10A026. American Society of Mechanical Engineers, 2022.

[28] Rodolfo Claren and Giorgio Diana. Mathematical analysis of transmission line vibration. *IEEE Transactions on power apparatus and systems*, (12):1741–1771, 1969.

[29] S. Cunha. Pipeline viv: Analytical solution, experiments and parameter identification. 01 2009.

[30] East Bay Times. Pge plan to bury power lines gets price tag; who will foot the bill?, Feb 2022. https://www.eastbaytimes.com/2022/02/10/pge-plan-to-bury-power-lines-gets-more-expensive-who-will-foot-the-bill/, Accessed on 2022-09-18.

[31] US EPRI and EDF R&D. Profiling and mapping of intelligent grid r&d programs. Technical report, Palo Alto, CA: US EPRI, 2006.

[32] Jixiong Fei, Bin Lin, Shuai Yan, Mei Ding, Juliang Xiao, Jin Zhang, Xiaofeng Zhang, Chunhui Ji, and Tianyi Sui. Chatter mitigation using moving damper. *Journal of Sound and Vibration*, 410:49–63, 2017.

[33] Yuan Gao, Guangming Song, Songtao Li, Fushuai Zhen, Dabing Chen, and Aiguo Song. Linespyx: A power line inspection robot based on digital radiography. *IEEE Robotics and Automation Letters*, 5(3):4759–4765, 2020.

[34] Chiara Gazzola, Francesco Foti, Luca Martinelli, and Federico Perotti. An appraisal of modelling strategies for assessing aeolian vibrations of transmission lines. In *24th Conference of the Italian Association of Theoretical and Applied Mechanics, AIMETA 2019*, pages 1522–1534. Springer, 2020.

[35] Bertrand Godard, Suzanne Guerard, and Jean-Louis Lilien. Original real-time observations of aeolian vibrations on power-line conductors. *IEEE transactions on power delivery*, 26(4):2111–2117, 2011.

[36] Suzanne Guérard, Jean-Louis Lilien, et al. Evaluation of power line cable fatigue parameters based on measurements on a laboratory cable test span. In *EIght International symposium on Cable Dynamics, ISCD 2009*, page 125. AIM, rue St Gilles, 31, 2009.

[37] Suzanne Guerard, Bertrand Godard, and Jean-Louis Lilien. Aeolian vibrations on power-line conductors, evaluation of actual self damping. *IEEE transactions on power delivery*, 26(4):2118–2122, 2011.

[38] Kunpeng Ji, Bin Liu, Jingchao Wang, Peng Li, Danyu Li, Lichun Zhang, Jingshan Han, and Yifeng Wang. Aeolian vibration and its suppression methods of long crossing span overhead electric transmission line. In *2019 6th International Conference on Information Science and Control Engineering (ICISCE)*, pages 663–667. IEEE, 2019.

[39] Paul Kakou and Oumar Barry. Simultaneous vibration reduction and energy harvesting of a nonlinear oscillator using a nonlinear electromagnetic vibration absorber-inerter. *Mechanical Systems and Signal Processing*, 156:107607, 2021.

[40] Paul Kakou, Mohammad Bukhari, Jiamin Wang, and Oumar Barry. On the vibration suppression of power lines using mobile damping robots. *Engineering Structures*, 239: 112312, 2021.

[41] Paul-Camille Kakou. *Towards A Mobile Damping Robot For Vibration Reduction of Power Lines*. PhD thesis, Virginia Tech, 2021.

[42] Paul-Camille Kakou and Oumar Barry. Toward a mobile robot for vibration control and inspection of power lines. *ASME Letters in Dynamic Systems and Control*, 2(1): 011001, 2021.

[43] Jaka Katrasnik, Franjo Pernus, and Bostjan Likar. A survey of mobile robots for distribution power line inspection. *IEEE Transactions on power delivery*, 25(1):485–493, 2009.

[44] Kreuzschnabel. Groß-rohrheim, 380 kv powerline from biblis nuclear power plant to

pfungstadt substation, May 2013. https://upload.wikimedia.org/wikipedia/commons/0/02/Freileitung-Ried-1.jpg, Accessed on 2023-01-10.

[45] YD Kubelwa, RC Loubser, and P Moodley. Experimental investigations of bending stresses of acsr conductors due to aeolian vibrations. In *Cigre Science & Engineering*, volume 9, pages 1286–1146. Innovation in the power systems industry, 2017.

[46] Peter H Larsen. A method to estimate the costs and benefits of undergrounding electricity transmission and distribution lines. *Energy Economics*, 60:47–61, 2016.

[47] Eduardo José Lima, Marcelo Henrique Souza Bomfim, and Miguel Augusto de Miranda Mourão. Polibot–power lines inspection robot. *Industrial Robot: An International Journal*, 2018.

[48] ML Lu and JK Chan. An efficient algorithm for aeolian vibration of single conductor with multiple dampers. *IEEE Transactions on power Delivery*, 22(3):1822–1829, 2007.

[49] Rebecca Miller, Farshid Abbasi, and Javad Mohammadpour. Power line robotic device for overhead line inspection and maintenance. *Industrial Robot: An International Journal*, 2017.

[50] MIT - Department of Ocean Engineering. 13.021 - marine hydrodynamics lecture 15, 2004. http://web.mit.edu/13.021/demos/lectures/lecture15.pdf, Accessed on 2023-01-10.

[51] Hyun Myung, Yang Wang, SC Kang, and XiaoQi Chen. Survey on robotics and automation technologies for civil infrastructure. 2014.

[52] NPR. Pg&e pleads guilty on 2018 california camp fire, Jun 2020. https://www.npr.org/2020/06/16/879008760/pg-e-pleads-guilty-on-2018-california-camp-fire-our-equipment-started-that-fire, Accessed on 2022-09-18.

[53] Mohammad B. Jiamin W. Paul, K. and B. Oumar. On the vibration suppression of power lines using mobile damping robots. *Engineering Structures, submitted*, 2020.

[54] PG&E. Electric transmission line inspection and preventive maintenance program, Jan 2020. https://www.pge.com/pge_global/common/pdfs/safety/emergency-preparedness/natural-disaster/wildfires/wildfire-mitigation-plan/reference-docs/TD-1001S.pdf, Accessed on 2022-09-18.

[55] Andrew Phillips, Eric Engdahl, Drew McGuire, Mark Major, and Glynn Bartlett. Autonomous overhead transmission line inspection robot (ti) development and demonstration. In *2012 2nd International Conference on Applied Robotics for the Power Industry (CARPI)*, pages 94–95. IEEE, 2012.

[56] Preformed Line Products. Aeolian vibration basics, Oct 2013. http://www.preformed.com/images/pdfs/Energy/Transmission/Motion_Control/VORTX_Vibration_Damper/EN-ML-1007-4AeolianViBook.pdf, Accessed on 2022-09-18.

[57] President's Council of Economic Advisers. Economic benefits of increasing electric grid resilience to weather outages., Mar 2017. https://www.energy.gov/sites/prod/files/2013/08/f2/Grid%20Resiliency%20Report_FINAL.pdf, Accessed on 2022-09-18.

[58] A Rezaei and MH Sadeghi. Analysis of aeolian vibrations of transmission line conductors and extraction of damper optimal placement with a comprehensive methodology. *International Journal of Engineering*, 32(2):328–337, 2019.

[59] Morteza Sadeghi and Aryo Rezaei. Aeolian vibrations of transmission line conductors with more than one damper. *International Journal of Engineering*, 28(10):1515–1524, 2015.

[60] US Energy Information Administration. Utilities continue to increase spending on the

electric transmission system, Mar 2021. https://www.eia.gov/todayinenergy/detail.php?id=47316, Accessed on 2022-09-18.

[61] Utility Products. Drones for power line inspections, Jan 2019. https://www.utilityproducts.com/line-construction-maintenance/article/16003823/drones-for-power-line-inspections, Accessed on 2022-09-18.

[62] Nitish Kumar Vaja, Oumar Barry, and Brian DeJong. Finite element modeling of stockbridge damper and vibration analysis: Equivalent cable stiffness. In *International Design Engineering Technical Conferences and Computers and Information in Engineering Conference*, volume 58226, page V008T12A012. American Society of Mechanical Engineers, 2017.

[63] NK Vaja, OR Barry, and EY Tanbour. On the modeling and analysis of a vibration absorber for overhead powerlines with multiple resonant frequencies. *Engineering Structures*, 175:711–720, 2018.

[64] Jack Vecchiarelli. *Aeolian vibration of a conductor with a Stockbridge-type damper*. PhD thesis, 1998.

[65] YR Wang and CY Lo. Design of hybrid dynamic balancer and vibration absorber. *Shock and Vibration*, 2014, 2014.

[66] Zhaoyang Wang, Qiang Gao, Jianbin Xu, and Dahua Li. A review of uav power line inspection. In Liang Yan, Haibin Duan, and Xiang Yu, editors, *Advances in Guidance, Navigation and Control*, pages 3147–3159. Springer Singapore, 2022. ISBN 978-981-15-8155-7.

[67] Liman Yang, Chenyao Fu, Yunhua Li, and Lianming Su. Survey and study on intelligent

monitoring and health management for large civil structure. *International Journal of Intelligent Robotics and Applications*, 3(3):239–254, 2019.

Appendices

Appendix A

Numerical Analysis Code (MATLAB)

```
clear all;
close all;
clc;

%% Cable Parameters

n=8; % Modes for approximation in ode45
mode = 8; % Excitation frequency
m = 0.349272076718; %mass per length in kg/m
L = 7.32; %length in m
mL = m*L; %mass in kg
T = 872; %tension in N
D = 0.0144; %diameter in m
E = 71e9; %Young's Modulus in N/m^2
I = (pi*D^4)/64; %Moment of Inertia in m^4
EI = E*I; %flexural rigidity in Nm^2

%% Computation

```

```
20 for i=1:3
21
22 [PB,PE,PR,PF,PM,loc]=nondim(n,T,L,m,EI,mode);
23 axialFrequency=PM(:,2);
24
25     if i==1
26         loc=0; % Cable Only
27     elseif i==2
28         loc=pi/2/axialFrequency(mode)*2; % Mass at node
29     else
30         loc=pi/2/axialFrequency(mode)*3; % Mass at antinode
31     end
32
33     % Initial conditions
34     [x0,tSpan]=iconds(PM,n,mode,loc);
35
36     % Solving the system
37     [tau,x]=ode45(@(tt,xx) modelfun(tt,xx,PB,PR,PE,PF,PM,mode,loc
          ),tSpan,x0);
38
39     % Cable Only
40     if i==1
41         % Time response of cable
42         qo=x(:,1:(end/2-3)); qodt=x(:,(end/2+1):(end-3));
43         % Time response of damper
```

```
44          qo2=x(:,(end/2-2):end/2-1); qo2dt=x(:,(end-2):end-1);
45
46      % Mass at node
47      elseif i==2
48          % Time response of cable
49          qn=x(:,1:(end/2-3)); qndt=x(:,(end/2+1):(end-3));
50          % Time response of damper
51          qn2=x(:,(end/2-2):end/2-1); qn2dt=x(:,(end-2):end-1);
52
53      % Mass at antinode
54      else
55          % Time response of cable
56          qa=x(:,1:(end/2-3)); qadt=x(:,(end/2+1):(end-3));
57          % Time response of damper
58          qa2=x(:,(end/2-2):end/2-1); qa2dt=x(:,(end-2):end-1);
59
60      end
61  end
62
63  %% Plot
64
65  Ls=linspace(0,L,1001);
66
67  LWave0=qo(:,:)*sqrt(2)*sin(axialFrequency(:)*Ls);
68  wave0r = rms(LWave0);
```

```
69
70 % figure(1)
71 % plot(Ls,wave0r,'k')
72
73 LWave1=qn(:,:)*sqrt(2)*sin(axialFrequency(:)*Ls);
74 wave1r = rms(LWave1);
75
76 % figure(2)
77 % plot(Ls,wave1r,'k')
78
79 LWave1=qa(:,:)*sqrt(2)*sin(axialFrequency(:)*Ls);
80 wave2r = rms(LWave1);
81
82 % figure(3)
83 % plot(Ls,wave2r,'k')
84
85 figure(4)
86 plot(Ls,wave0r*L,'k')
87 hold on
88 plot(Ls,wave1r*L,'r')
89 plot(Ls,wave2r*L,'b')
90 hold off
91 set(gca,'FontName','Times New Roman','FontSize',14)
92 xlabel('Normalized Length')
93 ylabel('Normalized Displacement')
```

```
94 legend('Cable Only','Mass at Node','Mass at Antinode')
95 xlim([pi/2/axialFrequency(mode) pi/2/axialFrequency(mode)*3])
96
97 %% Functions
98
99 function [x0,tSpan]=iconds(PM,n,mode,loc)
100         w=PM(:,1);
101
102         %Initial conditions
103         x0=zeros(2*n+4+2,1); x0(end/2-2)=loc;
104         t0=0;%initial time
105         tf=30;%final time
106         dt=1/(2*w(mode));%timestep
107         tSpan=t0:dt:tf;
108
109 end
110
111 function [ParamBeam,ParamE,ParamRobot,ParamF,ParamMode,loc]=
       nondim(n,T,L,m,EI,mode)
112
113 %Parameters of the mobile damping robot
114 mc=0.02;%in-span mass
115 ma=0.364;%suspended mass
116 b=0; % Inerter (not considered here)
117 kp=0;% Proportional gain (not considered here)
```

```
118 kd=0;% Derivative gain (not considered here)
119
120 % Parameters of the electromagnetic circuit
121 % Not considered here, but cannot be 0
122 R=0.000001;% resistance
123 Li=0.000001;% inductance
124 C=0.000001;% capacitance
125 q0=0.000001;%
126 v0=0.000001;
127
128 %Beam normalized parameters
129 wp=sqrt(EI/m)/L^2;
130 s=sqrt(T*L^2/EI);
131
132 w=zeros(n,1); % Natural frequency of each mode
133 axialFrequency=zeros(n,1); % Axial frequency of each mode
134 for iii=1:n
135     w(iii)=(pi)^2*sqrt(iii^4+iii^2*s^2/(pi^2)); %Natural
        frequency of the mode
136     axialFrequency(iii)=sqrt((-s^2/2+sqrt(s^4/4+w(iii)^2)));
137 end
138
139 k=1000; % Spring constant
140 kf=0;
141 kv=kf; % Voltage constant (Not considered)
```

```
142 Cd=0.1; % Damping constant
143
144 %Mobile damping robot normalized parameters
145 k=k*L^3/EI;
146 cd=Cd*L*sqrt(1/(m*EI));
147 %tau=0/L^2*sqrt(EI/m);
148 mc_=mc/m/L;
149 kp_=kp*L^3/EI;
150 kd_=kd*L/sqrt(m*EI);
151 ma_=ma/m/L;
152 b_=b/m/L;
153 va=0.1/v0;
154
155 %Electric circuit normalized parameters
156 kv_=kv*L/(Li*wp*q0);
157 kf_=kf*q0/sqrt(EI*m);
158 R_=R/(Li*wp);
159 C_=1/C/Li/wp^2;
160
161 d=0.028;
162 v=(w(mode)*wp)/2/pi*d/0.2;
163 rho=1.225;
164 cd_=3.2129;
165 f0=0.5*rho*d*cd_*v.^2;
166 amp_=f0*L^3/EI; %normalized amplitude
```

```
167 freq=w(mode)/2/pi*wp;
168
169 loc=pi/2/axialFrequency(mode)*2;
170
171 ParamBeam=[n;wp;s;L]; ParamE=[kv_;kf_;R_;C_]; ParamRobot=[k;cd;
       mc_;kp_;kd_;ma_;va;b_];
172 ParamF=[freq;amp_]; ParamMode=[w,axialFrequency];
173 end
174
175 function [xdt]=modelfun(t,x,ParamBeam,ParamRobot,ParamE,ParamF,
       ParamMode,mode,loc)
176
177 n=ParamBeam(1);
178 wp=ParamBeam(2);
179 % s=ParamBeam(3);
180 L=ParamBeam(4);
181
182 k=ParamRobot(1);
183 cd=ParamRobot(2);
184 %tau=0/L^2*sqrt(EI/m);
185 mc_=ParamRobot(3);
186 kp_=ParamRobot(4);
187 kd_=ParamRobot(5);
188 ma_=ParamRobot(6);
189 va=ParamRobot(7);
```

```
190 b_=ParamRobot(8);
191
192 kv_=ParamE(1);
193 kf_=ParamE(2);
194 R_=ParamE(3);
195 C_=ParamE(4);
196
197 freq=ParamF(1);
198 amp_=ParamF(2);
199
200 w=ParamMode(:,1);
201 axialFrequency=ParamMode(:,2);
202
203 FWind=sum(amp_.*sin(2*pi*freq*t/wp)); % Composed from various
       frequencies
204
205 xdt=zeros(2*n+4+2,1);
206 xdt(1:end/2,1)=x((end/2+1):end,1); % Displacement of the Cable
       Modes
207
208 q1=x(1:(end/2-3),1);
209 q1dt=x((end/2+1):(end-3),1);
210
211 q2=x((end/2-2):end/2-1,1);
212 q2dt=x((end-2):end-1,1);
```

```
213
214 q3=x((end/2),1);
215 q3dt=x(end,1);
216
217 % Eigenfunctions
218 phi=zeros(n,1);
219 phiInt=zeros(n,1);
220
221 for iii=1:n
222     phi(iii)=sqrt(2)*sin(axialFrequency(iii)*q2(1));
223     phiInt(iii)=-sqrt(2)/axialFrequency(iii)*(cos(axialFrequency(
            iii))-1);
224 end
225
226 pt_excite = L/2; % Location of the input excitation
227 phi_point_excite = zeros(n,1);
228 for iii=1:n
229     phi_point_excite(iii)=sqrt(2)*sin(axialFrequency(iii)*
            pt_excite);
230 end
231
232 p=loc; % Final robot position reference
233
234 disSum=q1.'*phi;
235 velSum=q1dt.'*phi;
```

```
236
237 zeta=0.001;
238
239 M1=eye(n)+1*mc_*(phi.*phi); % Beam inertia matrix
240 M2=diag([mc_,ma_+b_]); % Robot inertia matrix
241 q1ddt=M1\textbackslash(-(w.^2).*q1-2*zeta*(w.*q1dt)...
242           -(k*(disSum-q2(2))+cd*(velSum-q2dt(2))+kf_*q3dt(1))*phi
                + 0*FWind*phiInt +1*FWind*phi_point_excite);
243 q2ddt=M2\textbackslash[(kp_*(p-q2(1))+kd_*(-q2dt(1)));...
244           (k*(disSum-q2(2))+cd*(velSum-q2dt(2))+kf_*q3dt(1))];
245 q3ddt=(kv_*(velSum-q2dt(2))-R_*q3dt(1)-C_*q3(1));
246
247 xdt(end/2+1:end)=[q1ddt;q2ddt;q3ddt];
248
249 end
```

Appendix B

Continuous Sampling Code (Arduino)

```
#include <math.h>
#include <Wire.h>
#include <Adafruit_MMA8451.h>
#include <Adafruit_Sensor.h>
#include <DynamixelShield.h>

#if defined(ARDUINO_AVR_UNO) || defined(ARDUINO_AVR_MEGA2560)
  #include <SoftwareSerial.h>
  SoftwareSerial soft_serial(7, 8); // DYNAMIXELShield UART RX/TX
  #define DEBUG_SERIAL soft_serial
#elif defined(ARDUINO_SAM_DUE) || defined(ARDUINO_SAM_ZERO)
  #define DEBUG_SERIAL SerialUSB
#else
  #define DEBUG_SERIAL Serial
#endif

const uint8_t DXL_ID1 = 1; //first motor
const uint8_t DXL_ID2 = 2; //second motor
const float DXL_PROTOCOL_VERSION = 2.0;

DynamixelShield dxl;

using namespace ControlTableItem;

```

```
25 Adafruit_MMA8451 mma = Adafruit_MMA8451();
26
27 volatile bool sample = false;
28
29 void setup() {
30
31  delay(10000); // Delay to open Serial Monitor
32
33  //ACCELEROMETER SETUP
34   Serial.begin(115200);
35
36   Serial.println("Adafruit MMA8451 test!");
37
38   if (! mma.begin()) {
39     Serial.println("Couldnt start");
40     while (1);
41   }
42   Serial.println("MMA8451 found!");
43
44   mma.setRange(MMA8451_RANGE_8_G);
45
46   Serial.print("Range = "); Serial.print(2 << mma.getRange());
47   Serial.println("G");
48
49   // DYANMIXEL SETUP
50   DEBUG_SERIAL.begin(115200);
51
52   // Set Port baudrate to 57600bps. This has to match with DYNAMIXEL baudrate.
53   dxl.begin(57600);
54   // Set Port Protocol Version. This has to match with DYNAMIXEL protocol
         version.
```

```
55   dxl.setPortProtocolVersion(DXL_PROTOCOL_VERSION);
56   // Get DYNAMIXEL information
57   dxl.ping(DXL_ID1);
58   dxl.ping(DXL_ID2);
59
60   // Turn off torque when configuring items in EEPROM area
61   dxl.torqueOff(DXL_ID1);
62   dxl.setOperatingMode(DXL_ID1, OP_VELOCITY);
63   dxl.torqueOn(DXL_ID1);
64   dxl.torqueOff(DXL_ID2);
65   dxl.setOperatingMode(DXL_ID2, OP_VELOCITY);
66   dxl.torqueOn(DXL_ID2);
67
68 /////////// Courtesy of MartinL on Arduino Forum (https://forum.arduino.cc/t/
       how-to-implement-timer-interrupt-on-mkr-1010/610137/2)
69
70 // Setting Timer4 for ISR
71  GCLK->CLKCTRL.reg = GCLK_CLKCTRL_CLKEN |                    // Enable GCLK0 for
       TC4 and TC5
72                      GCLK_CLKCTRL_GEN_GCLK0 |                // Select GCLK0 at
                           48MHz
73                      GCLK_CLKCTRL_ID_TC4_TC5;                // Feed GCLK0
                           output to TC4 and TC5
74   while (GCLK->STATUS.bit.SYNCBUSY);                         // Wait for
       synchronization
75
76   TC4->COUNT16.CC[0].reg = 29999;                            // Set the TC4 CC0
       register as the TOP value in match frequency mode
77   while (TC4->COUNT16.STATUS.bit.SYNCBUSY);                  // Wait for
       synchronization
78
```

```
79   NVIC_SetPriority(TC4_IRQn, 0);     // Set the Nested Vector Interrupt
         Controller (NVIC) priority for TC4 to 0 (highest)
80   NVIC_EnableIRQ(TC4_IRQn);          // Connect TC4 to Nested Vector Interrupt
         Controller (NVIC)
81
82   TC4->COUNT16.INTENSET.reg = TC_INTENSET_OVF;              // Enable TC4
         overflow (OVF) interrupts
83
84   TC4->COUNT16.CTRLA.reg |= TC_CTRLA_PRESCSYNC_PRESC |      // Reset timer on
         the next prescaler clock
85                             TC_CTRLA_PRESCALER_DIV8 |       // Set prescaler to
                                   8, 48MHz/8 = 6MHz
86                             TC_CTRLA_WAVEGEN_MFRQ |         // Put the timer
                                  TC4 into match frequency (MFRQ) mode
87                             TC_CTRLA_MODE_COUNT16;          // Set the timer to
                                   16-bit mode
88   while (TC4->COUNT16.STATUS.bit.SYNCBUSY);                 // Wait for
         synchronization
89
90   TC4->COUNT16.CTRLA.bit.ENABLE = 1;                        // Enable the TC4
         timer
91   while (TC4->COUNT16.STATUS.bit.SYNCBUSY);                 // Wait for
         synchronization
92
93 /////////
94
95   Serial.println("Entering Loop");
96
97   //both wheels spinning in opposite directions
98   dxl.setGoalVelocity(DXL_ID1, 10, UNIT_RPM);
99   dxl.setGoalVelocity(DXL_ID2, -10, UNIT_RPM);
```

```
100
101 }
102
103 void loop() {
104
105 if (sample = true) {
106   mma.read();
107   sensors_event_t event;
108   mma.getEvent(&event);
109   Serial.println(event.acceleration.z);
110
111   sample = false;
112 }
113
114 }
115
116 // ISR for Uniform Sample Rate
117 void TC4_Handler()
118 {
119     sample = true;
120     TC4->COUNT16.INTFLAG.reg = TC_INTFLAG_OVF; // Clear interrupt flag
121 }
```

Appendix C

Antinode Tracking Code (Arduino)

```
1  //TRACKS ANTINODE USING RMS
2
3  #include <math.h>
4  #include <Wire.h>
5  #include <Adafruit_MMA8451.h>
6  #include <Adafruit_Sensor.h>
7  #include <DynamixelShield.h>
8
9  #if defined(ARDUINO_AVR_UNO) || defined(ARDUINO_AVR_MEGA2560)
10   #include <SoftwareSerial.h>
11   SoftwareSerial soft_serial(7, 8); // DYNAMIXELShield UART RX/TX
12   #define DEBUG_SERIAL soft_serial
13 #elif defined(ARDUINO_SAM_DUE) || defined(ARDUINO_SAM_ZERO)
14   #define DEBUG_SERIAL SerialUSB
15 #else
16   #define DEBUG_SERIAL Serial
17 #endif
18
19 const uint8_t DXL_ID1 = 1; //first motor
20 const uint8_t DXL_ID2 = 2; //second motor
21 const float DXL_PROTOCOL_VERSION = 2.0;
22
23 DynamixelShield dxl;
24
```

```
25 using namespace ControlTableItem;
26
27 Adafruit_MMA8451 mma = Adafruit_MMA8451();
28
29 //starting position of robot
30 //int basepos = 0;
31
32 //sets effective wheel radius in mm
33 //double r_wheel = 10;
34
35 //sets travel per rev in cm
36 //double C = 2*PI*r_wheel;
37
38 //sets travel distance per iteration in inches
39 //int testDistance = 3*2.54;
40
41 //sets travel distance per iteration in revs
42 //int testRevs = testDistance/C;
43
44 //sets RPM of motors
45 int rpm = 30;
46
47 //sets time for wheels to turn
48 //timeStep = round(rpm/60/testRevs*1000);
49 int timeStep = 3000;
50 //sets time for delay to reach new steady state after robot moves
51 int SSdelay = 3000;
52
53 //initializes variable at initialvalue
54 //double currentpos = basepos;
55
```

```
56 //creates baseline acceleration values
57 double previousRMS = 0;
58 double currentRMS = 0;
59 double sum = 0;
60
61 //set directional multiplier
62 int DM = 1;
63
64 //number of acceleration values to sample
65 const unsigned int samples = 200;
66 //array to store those values
67 double accelVals[samples];
68 //margin to prevent recursion and unnecessary movement due to slight increases
       in acceleration
69 //need to change this to maybe be variable so it changes based on different
     gains?
70 //the lower the more sensitive, so more likely to get there, but also more
     likely to move recursively
71 double margin = 0.2;
72
73 void setup() {
74
75  delay(5000);
76
77  //ACCELEROMETER SETUP
78    Serial.begin(115200);
79
80    Serial.println("Adafruit MMA8451 test!");
81
82    if (! mma.begin()) {
83      Serial.println("Couldnt start");
```

```
84      while (1);
85    }
86    Serial.println("MMA8451 found!");
87
88    mma.setRange(MMA8451_RANGE_8_G);
89
90    Serial.print("Range = "); Serial.print(2 << mma.getRange());
91    Serial.println("G");
92
93    // DYANMIXEL SETUP
94    // For Uno, Nano, Mini, and Mega, use UART port of DYNAMIXEL Shield to debug
          .
95    DEBUG_SERIAL.begin(115200);
96
97    // Set Port baudrate to 57600bps. This has to match with DYNAMIXEL baudrate.
98    dxl.begin(57600);
99    // Set Port Protocol Version. This has to match with DYNAMIXEL protocol
          version.
100   dxl.setPortProtocolVersion(DXL_PROTOCOL_VERSION);
101   // Get DYNAMIXEL information
102   dxl.ping(DXL_ID1);
103   dxl.ping(DXL_ID2);
104
105   // Turn off torque when configuring items in EEPROM area
106   dxl.torqueOff(DXL_ID1);
107   dxl.setOperatingMode(DXL_ID1, OP_VELOCITY);
108   dxl.torqueOn(DXL_ID1);
109   dxl.torqueOff(DXL_ID2);
110   dxl.setOperatingMode(DXL_ID2, OP_VELOCITY);
111   dxl.torqueOn(DXL_ID2);
112
```

```
113   //take initial sample
114   Serial.println("Taking Initial Sample");
115
116   //takes and stores acceleration samples
117   for (int i=0; i<samples; i++) {
118      mma.read();
119      sensors_event_t event;
120      mma.getEvent(&event);
121      accelVals[i] = abs(event.orientation.z); //technically unecessary if
             squaring, but doesn't make a difference
122   }
123
124   //finds RMS of the initial sample set
125   for (int j=0; j<samples; j++) {
126     accelVals[j] = accelVals[j]*accelVals[j]; //squares each element in the
         array
127   }
128   for (int k=0; k<samples; k++) {
129     sum = sum + accelVals[k]; //sums the squares
130   }
131   previousRMS = sqrt(sum/samples);
132
133   Serial.print("Initial RMS value is ");
134   Serial.println(previousRMS);
135
136   //move in arbitrary direction for first sample in loop to be comparative
137   //both wheels spinning in opposite directions
138   dxl.setGoalVelocity(DXL_ID1, DM*rpm, UNIT_RPM);
139   dxl.setGoalVelocity(DXL_ID2, -1*DM*rpm, UNIT_RPM);
140   //moves for designated amount of time
141   delay(timeStep);
```

```
142   //outputs motor settings for reference
143   DEBUG_SERIAL.println("Present Velocity(rpm) Motor 1: ");
144   DEBUG_SERIAL.print(dxl.getPresentVelocity(DXL_ID1, UNIT_RPM));
145   DEBUG_SERIAL.println("Present Velocity(rpm) Motor 2: ");
146   DEBUG_SERIAL.print(dxl.getPresentVelocity(DXL_ID2, UNIT_RPM));
147   //turns off motors
148   dxl.setGoalVelocity(DXL_ID1, 0, UNIT_RPM);
149   dxl.setGoalVelocity(DXL_ID2, 0, UNIT_RPM);
150   //waits for transient response to clear before taking new samples
151   delay(SSdelay);
152
153   Serial.println("Entering Loop");
154 }
155
156 void loop() {
157
158   sum = 0;
159
160   Serial.println("Taking Sample");
161
162   //takes and stores acceleration samples
163   for (int i=0; i<samples; i++) {
164      mma.read();
165      sensors_event_t event;
166      mma.getEvent(&event);
167      accelVals[i] = abs(event.orientation.z);
168   }
169
170   //finds RMS of the sample set
171   for (int j=0; j<samples; j++) {
```

```
172     accelVals[j] = accelVals[j]*accelVals[j]; //squares each element in the
            array
173   }
174   for (int k=0; k<samples; k++) {
175     sum = sum + accelVals[k]; //sums the squares
176   }
177   currentRMS = sqrt(sum/samples);
178
179   Serial.print("Current RMS value is ");
180   Serial.println(currentRMS);
181
182   //CASE 1: acceleration increases (indicates movement toward antinode)
183   if (currentRMS > (previousRMS + margin)) {
184     //sets new global max for next comparison
185     previousRMS = currentRMS;
186
187     Serial.println("Moved TOWARD Antinode");
188
189     //no need to change DM -> keep going same direction
190
191     //both wheels spinning in opposite directions
192     dxl.setGoalVelocity(DXL_ID1, DM*rpm, UNIT_RPM);
193     dxl.setGoalVelocity(DXL_ID2, -1*DM*rpm, UNIT_RPM);
194     //moves for designated amount of time
195     delay(timeStep);
196 //     DEBUG_SERIAL.print("Present Velocity(rpm) Motor 1: ");
197 //     DEBUG_SERIAL.println(dxl.getPresentVelocity(DXL_ID1, UNIT_RPM));
198 //     DEBUG_SERIAL.print("Present Velocity(rpm) Motor 2: ");
199 //     DEBUG_SERIAL.println(dxl.getPresentVelocity(DXL_ID2, UNIT_RPM));
200 //     delay(1000);
201     //turns off motors
```

```
202       dxl.setGoalVelocity(DXL_ID1, 0, UNIT_RPM);
203       dxl.setGoalVelocity(DXL_ID2, 0, UNIT_RPM);
204       //waits for transient response to clear before taking new samples
205       delay(SSdelay);
206     }
207
208     //CASE 2: acceleration decreases (indicates movement from antinode)
209     else if (currentRMS < (previousRMS - margin)) {
210       //sets new global max for next comparison
211       previousRMS = currentRMS;
212
213       Serial.println("Moved AWAY FROM Antinode");
214
215       //need to change DM -> go in opposite direction
216       DM = -1*DM;
217
218       //both wheels spinning in opposite directions
219       dxl.setGoalVelocity(DXL_ID1, DM*rpm, UNIT_RPM);
220       dxl.setGoalVelocity(DXL_ID2, -1*DM*rpm, UNIT_RPM);
221       delay(timeStep);
222 //    DEBUG_SERIAL.print("Present Velocity(rpm) Motor 1: ");
223 //    DEBUG_SERIAL.println(dxl.getPresentVelocity(DXL_ID1, UNIT_RPM));
224 //    DEBUG_SERIAL.print("Present Velocity(rpm) Motor 2: ");
225 //    DEBUG_SERIAL.println(dxl.getPresentVelocity(DXL_ID2, UNIT_RPM));
226 //    delay(1000);
227       //turns off motors
228       dxl.setGoalVelocity(DXL_ID1, 0, UNIT_RPM);
229       dxl.setGoalVelocity(DXL_ID2, 0, UNIT_RPM);
230       delay(SSdelay);
231     }
232
```

```
233   //CASE 3: acceleration stays roughly the same (at antinode position)
234   else {
235     //don't really have to move anymore
236     Serial.println("Reached Antinode");
237     //sets new global max for next comparison
238 //     previousRMS = currentRMS;
239 
240     delay(SSdelay);
241     }
242 }
```

Appendix D

Arduino Serial Monitor Readout During Navigation

Adafruit MMA8451 test!

MMA8451 found!

Range = 8G

Taking Initial Sample

Initial RMS value is 11.80

Present Velocity(rpm) Motor 1: 29.31

Present Velocity(rpm) Motor 2: -30.00

Entering Loop

Taking Sample

Current RMS value is 12.46

Moved TOWARD Antinode

Taking Sample

Current RMS value is 13.14

Moved TOWARD Antinode

Taking Sample

Current RMS value is 14.00

Moved TOWARD Antinode

Taking Sample

Current RMS value is 14.27

Moved TOWARD Antinode

Taking Sample

Current RMS value is 14.68

Moved TOWARD Antinode

Taking Sample

Current RMS value is 14.85

Reached Antinode

Taking Sample

Current RMS value is 14.89

Moved TOWARD Antinode

Taking Sample

Current RMS value is 16.53

Moved TOWARD Antinode

Taking Sample

Current RMS value is 17.45

Moved TOWARD Antinode

Taking Sample

Current RMS value is 18.51

Moved TOWARD Antinode

Taking Sample

Current RMS value is 14.90

Moved AWAY FROM Antinode

Taking Sample

Current RMS value is 18.59

Moved TOWARD Antinode